Acetylation regulates the oligomerization state and activity of RNase J, the major ribonuclease of *Helicobacter pylori*

Alejandro TEJADA-ARRANZ[1,2,+], Maxime BOUILLOUX-LAFONT[1], Xue-Yuan PEI[3], Thibaut DOUCHÉ[4], Mariette MATONDO[4], Allison WILLIAMS[5], Bertrand RAYNAL[6], Ben F LUISI[3] and Hilde DE REUSE[1]*

[1] Unité Pathogenèse de *Helicobacter*, CNRS UMR2001, Département de Microbiologie, Institut Pasteur, Paris, France.

[2] Université de Paris, Sorbonne Paris Cité, Paris, France.

[3] Department of Biochemistry, University of Cambridge, Tennis Court Road, Cambridge CB2 1GA, UK.

[4] Plateforme Protéomique, Unité de Spectrométrie de Masse pour la Biologie, C2RT, USR CNRS 2000, Institut Pasteur, Paris, France.

[5] University of California San Francisco, Cellular Molecular Pharmacology School, School of Medicine, San Francisco CA, USA

[6] Plateforme de biophysique moléculaire, Département de Biologie structurale et chimie, Institut Pasteur, Paris, France.

+ Present address: Biozentrum, University of Basel, Switzerland

*Corresponding author: hdereuse@pasteur.fr
Institut Pasteur, Unité Pathogenèse de *Helicobacter*
28, rue du Docteur Roux
75724 PARIS Cedex 15 FRANCE
Tel: +33 1 40 61 36 41

Abstract

In the pathogenic bacterium *Helicobacter pylori*, post-transcriptional regulation is dominated by the activity of a protein complex, known as the RNA degradosome, composed of the essential ribonuclease RNase J and the DEAD-box RNA helicase RhpA. Here, we describe post-translational modifications of this protein complex that affect its activity. Cell-extracted RNase J is acetylated on multiple residues, one of which, K649, impacts strongly on RNase J oligomerization, which in turn influences recruitment into the degradosome and ribonuclease activity. Corroborating the link between oligomerization and activity, mutations targeting K649 and other residues affect the dimerization and *in vitro* activity of RNase J. Our crystal structure of RNase J reveals loops that gate access to the active site and rationalizes how oligomerization state influences activity. We show that the acetylated residues of RNase J are important for *H. pylori* morphology, highlighting that the modifications affect the cellular function of RNase J. We propose acetylation as a regulatory level controlling the activity of RNase J and the *H. pylori* RNA degradosome.

Introduction

Post-transcriptional regulation is one of the most important levels of control of gene expression in every kingdom of life. Ribonucleases (RNases) are key enzymes in this regulation, that are involved in RNA maturation and degradation. In several bacteria, major RNases act in concert with DEAD-box RNA helicases, that help to unfold RNA secondary structures, within protein machines called RNA degradosomes (Tejada-Arranz et al., 2020a).

We previously demonstrated the existence of a minimal RNA degradosome in *Helicobacter pylori* (Redko et al., 2013). This Gram-negative bacterial pathogen chronically colonizes the stomach of half of the human population worldwide. Infection leads to chronic gastritis and, in some cases, to further gastric pathologies such as peptic ulcers, MALT lymphoma, or gastric adenocarcinoma that causes 800,000 deaths each year worldwide (Amieva and Peek, 2016). *H. pylori* possesses a small genome (1.6 Mb) with few transcriptional regulators, and several lines of evidence indicate that post-transcriptional regulation plays a major role in gene expression control in this organism (Eisenbart et al., 2020; Sharma et al., 2010; Tejada-Arranz and De Reuse, 2021). The *H. pylori* RNA degradosome is composed of RNase J, a 77.6 kDa enzyme that possesses both 5'-3' exoribonuclease and endoribonuclease activities, and RhpA, a DEAD-box RNA helicase, with a molecular weight of 55.8 kDa (El Mortaji et al., 2018; Redko et al., 2013). RNase J is essential in *H. pylori* and plays a major role in the degradation of both mRNAs and antisense RNAs (Redko et al., 2016). RhpA is the sole DEAD-box RNA helicase encoded by the *H. pylori* genome and is essential for colonization in the mouse infection model (El Mortaji et al., 2018). Furthermore, we recently demonstrated that, in *H. pylori*, the RNA degradosome is compartmentalized into clusters at the inner membrane whose formation is regulated and likely represents a major level of control of its activity (Tejada-Arranz et al., 2020b).

RNase J-encoding genes are present in 57 % of sequenced bacteria (Tejada-Arranz et al., 2020a), including the Gram-positive organisms *Bacillus subtilis*, *Staphylococcus aureus* and *Deinococcus radiodurans*. *B. subtilis* and *S. aureus* encode two paralogues of RNase J, called J1 and J2 while *H. pylori, Streptomyces pyogenes* and *D. radiodurans* possess only one gene for this protein. Compared to the RNase J proteins of these three organisms, the *H. pylori*

83 enzyme possesses a unique N-terminal extension of 132 residues that is
84 predicted to be predominantly disordered (Redko et al., 2013; Tejada-Arranz et
85 al., 2020b). In *B. subtilis*, while both RNase J paralogues have equivalent
86 endoribonuclease activities, RNase J2 seems to lack the 5'-3' exoribonuclease
87 activity that predominates in RNase J1 (Mathy et al., 2010). Furthermore, these
88 two proteins interact and form a complex that has different cleavage specificity *in*
89 *vitro* than each protein alone (Mathy et al., 2010). *B. subtilis* RNases J1 and J2
90 (*Bsu*RNases J1 and J2) form a heterotetramer *in vitro* (Mathy et al., 2010). *In*
91 *vitro* analysis of the RNase J1 enzyme from *S. aureus* showed that it
92 predominantly assembles into dimers, but also forms tetramers, independently of
93 divalent cations (Hausmann et al., 2017a). The single RNase J from *S. pyogenes*
94 forms dimers and tetramers *in vitro* without divalent cations being observed in the
95 dimerization surface (Pei et al., 2015). In *D. radiodurans*, RNase J forms a dimer
96 in a Mn-dependent fashion *in vitro*, and the interaction between the two
97 monomers is mediated by the C-terminal domain of *Dra*RNase J (Zhao et al.,
98 2015). Several crystal structures of RNase J proteins have been published
99 (Newman et al., 2011; Pei et al., 2015; Zhao et al., 2015), where RNase J is
100 generally found to be a tetramer (dimer of dimers). However, it is unknown
101 whether the different oligomeric states of RNase J detected *in vitro* have
102 differences in activity.

103 Almost nothing is known about post-translational modification of these protein
104 complexes and whether this might influence their activity. Acetylation has
105 emerged as a major post-translational regulatory mechanism in bacteria
106 (Carabetta and Cristea, 2017; Wolfe, 2016). Although the acetylation of lysine,
107 cysteine, serine and threonine residues has been reported, lysine acetylation is
108 the most prominent modification, particularly on its ε-amino group (Wolfe, 2016).
109 This modification has been shown to regulate multiple properties of the target
110 proteins, including enzymatic activity, DNA-binding capability or stability, among
111 others (Carabetta and Cristea, 2017). Interestingly, some proteins involved in
112 RNA metabolism have been reported to be lysine acetylated, including (i)
113 *Escherichia coli* RNase R, whose acetylation regulates its stability (Liang et al.,
114 2011); (ii) *E. coli* RNase II, regulated at the activity level (Song et al., 2016); and
115 (iii) the CshA DEAD-box RNA helicase from *B. subtilis*, where acetylation has
116 been proposed to influence its interaction with RNA polymerase independently

117 from its association with RNase Y, the major ribonuclease of the *B. subtilis* RNA
118 degradosome (Ogura and Asai, 2016).
119 The central importance of RNase J in post-transcriptional regulation in *H. pylori*
120 and its participation in an RNase J-based degradosome prompted us to
121 investigate the structure, oligomeric state and post-translational regulation of the
122 *H. pylori* RNase J and to assess its stoichiometry in the RNA degradosome. Here,
123 we report the crystal structure of *H. pylori* RNase J without its N-terminal
124 extension. We also showed that RNase J is in equilibrium between monomeric
125 and dimeric states *in vitro* and that, together with its monomeric RNA helicase
126 partner RhpA, assembles into a minimal degradosome complex with a 1:1
127 stoichiometry. Our data suggest that the dimeric form constitutes the active form
128 of RNase J *in vitro*. Furthermore, we found for the first time that RNase J is
129 acetylated at several residues by multiple mechanisms. We concluded that the
130 acetylation state regulates the oligomerization state and activity of RNase J *in*
131 *vitro* and its activity in *H. pylori*, and thereby constitutes an important level of
132 control of the RNA degradosome.
133

Results

Structure of the *H. pylori* RNase J

Several attempts to purify sufficient amounts of full-length RNase J from *H. pylori* to obtain crystals were unsuccessful. As we previously reported (Tejada-Arranz et al., 2020b), the N-terminal part of RNase J (first 120 amino acids) that is specific of the *Helicobacter* species is predicted to be an intrinsically disordered region (IDR). After truncating this region, well diffracting crystals were obtained from this RNase J form comprising residues 137-691 (from *H. pylori* strain 26695, uniprot P56185). The crystal structure of *H. pylori* RNase J was solved at 2.75 Å by molecular replacement using the *Streptomyces coelicolor* homologue as a search model (Table S1). One molecule occupies the asymmetric unit of the crystal, and through crystal symmetry a homotetramer can be generated that is organized as a dimer-of-dimers (Figure 1A). The core region of the enzyme, residues 137-586, encompasses the beta-CASP and beta-lactamase domains that define this family (Callebaut et al., 2002), but there are no detectable metal cofactors in the map at the catalytic site. An X-ray Zn-peak scan also confirmed that there are no detectable Zn ions in the crystal.

The structure predicted by the Robetta server, based on machine learning (Baek et al., 2021), is in excellent agreement with the X-ray model for the core, with the notable exception of the three loop regions 174-183, 431-441 and 575-586 at the entrance to the active site, for which the predicted loop positions are closer to those seen in the crystal structure of the *S. coelicolor* RNase J (Figure 1B-C). The electron density over these regions is well defined in the *H. pylori* map and modelled with high confidence. Comparing the structures, it is apparent that the position of the loops will enforce a different path for the RNA substrate in *H. pylori* RNase J compared with the *S. coelicolor* enzyme (Figure 1C).

The C-terminal domain, from residues 587 to 691, is poorly ordered in the crystal lattice and the density was not sufficiently well resolved to model the polypeptide. The Robetta model for the C-terminal domain fits well and fitted into the map, showing good agreement with the predicted helical segments. The predicted model is also in agreement with a high confidence homology model prepared by PHYRE2 using the *Thermus thermophilus* homolog as template (PDB 3BK2). This domain makes a self-complementary interaction through

168 crystal lattice contact. The Robetta model predicted with low confidence an
169 extended helical region of the N-terminal residues 1-136 that were not included
170 in the crystallized protein, and this region seems unlikely to have a compact fold.
171 The final model to fit the X-ray data is a fusion of the fitted crystal structure of the
172 core and the Robetta model for the C-terminal domain with side chains removed
173 due to poor resolution of this part of the electron density map.

174 In the dimeric unit, the protomer interfaces are formed by self-complementary
175 interactions made mostly by the CTD. The surface area buried at the CTD-CTD
176 interface is estimated to be 1165 $Å^2$. The beta-CASP and beta-lactamase
177 domains of RNase J also make a self-complementary interface in the principal
178 dimer, with an estimated area of 672 $Å^2$ that is a little more than half of the CTD-
179 CTD contribution. Stronger interactions typically have a surface area of more than
180 2000 $Å^2$ (Nooren and Thornton, 2003). The interface between the beta-CASP
181 and beta-lactamase domains is very similar to that seen in other dimers of RNase
182 J, for instance in the homologue of *S. coelicolor* (Pei et al., 2015). The interfaces
183 that are formed between the dimer units to make the tetramer are also made by
184 the beta-CASP and beta-lactamase interfaces, and these have a total buried area
185 of 2070 $Å^2$.

186 An overlay of RNase J of *H. pylori* and of *S. coelicolor*, where an RNA substrate
187 is bound, suggests that the path of the RNA to the active site cannot be the same
188 for the two enzymes, and that the nucleic acid would need to be rerouted in the
189 *H. pylori* enzyme. The obstructions are caused by exposed peptide loop regions
190 that are positioned to accommodate the CTD. It is possible that changes in the
191 oligomerization state will impact on the loops and access to the active site.

192 It is notable that the CTD has extensive charged side chains on the surface of
193 proteins that likely form complementary charge interactions. Such an
194 organization may stabilize the fold of the small domain (Perutz, 1978; Perutz and
195 Raidt, 1975; Zhou and Pang, 2018). As the self-complementary interactions of
196 the C-terminal domain are a key component of the assembly, any changes in the
197 stability of the CTD may impact on the oligomeric state. We will return to this point
198 below when discussing the structural impact of modification of the surface
199 exposed residues.

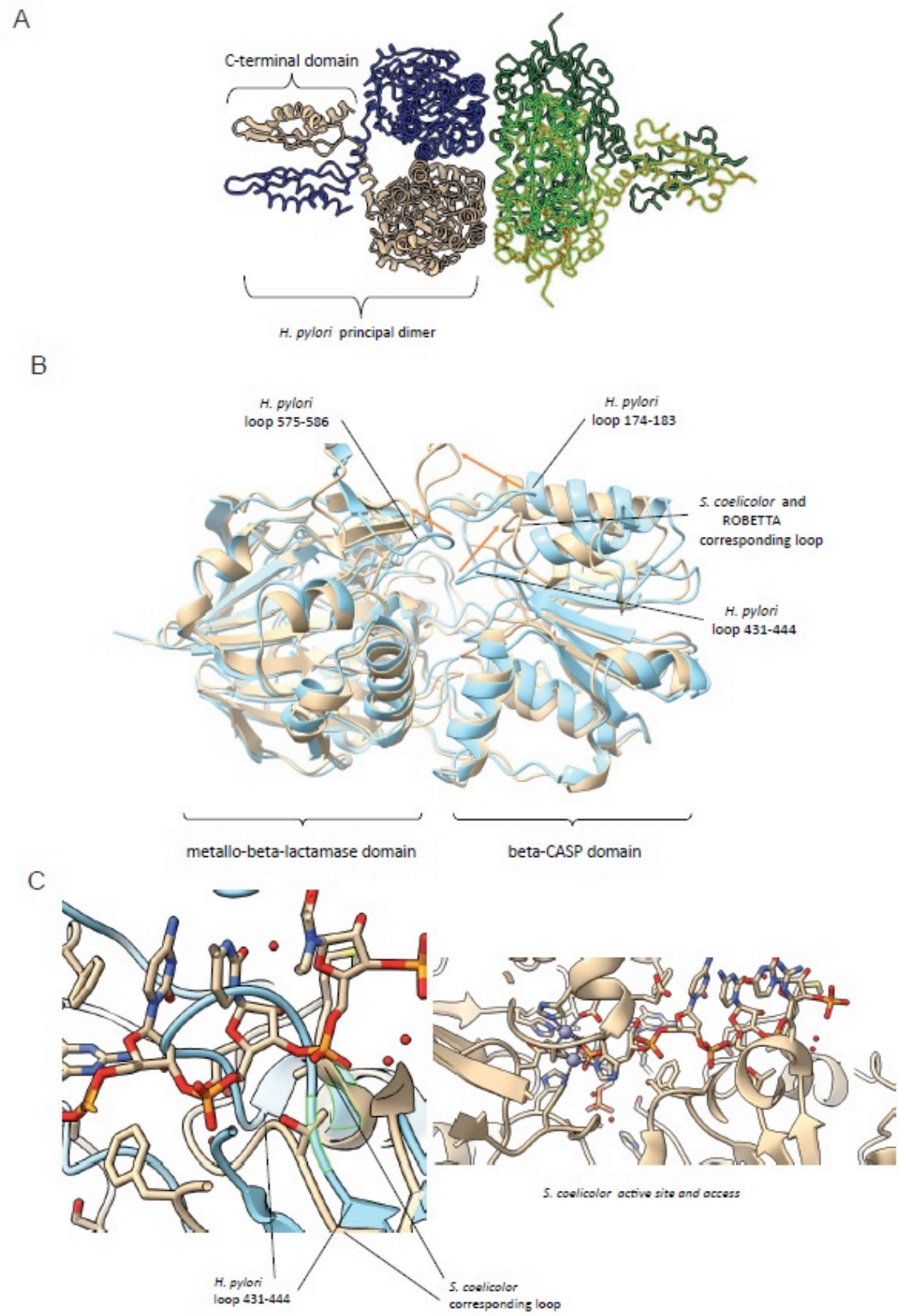

Figure 1 Structure of RNase J from *H. pylori.* Crystals were prepared from *H. pylori* RNase J residues 139-691, encompassing the beta-CASP, metallo-beta-lactamase and C-terminal domains. (A) View of the tetramer, which is a dimer-of-dimers. A monomer occupies the asymmetric unit, and the tetramer is generated through crystallographic symmetry. (B) Overlay

205 of the predicted structure from Robetta server (beige) and the refined crystal structure (blue). The
206 individual beta-CASP and metallo-beta-lactamase domains overlay well, but there are noted
207 differences in the orientation of the three loop regions 174-183, 431-441 and 575-586 at the
208 entrance to the active site (shifts indicated by orange arrows). The predicted structure is closer to
209 the orientation seen in *Streptomyces coelicolor* RNase J, shown in overlay with *H. pylori* enzyme
210 in the left panel of (C). The *S. coelicolor* enzyme structure (beige) is in complex with RNA, and
211 the path of the RNA substrate along a channel to the active site in shown in the right panel. The
212 *H. pylori* RNase J (blue) cannot bind RNA with the same orientation seen for the *S. coelicolor*
213 enzyme due to steric clashes with the loops (left panel). The two zinc ions at the active site of the
214 *S. coelicolor* enzyme are indicated in the right panel.
215

216 **_In vitro_ analysis of the oligomeric state of the two partners of the _H. pylori_**
217 **RNA degradosome**

218 Several crystal structures of RNase J proteins described to date correspond
219 to tetramers. However, other oligomeric states (dimers and monomers) were
220 found in solution and the activity of the different forms was unclear. Therefore,
221 we decided to evaluate the oligomeric state of RNase J and RhpA *in vitro*. For
222 that, His-tagged versions of RNase J and RhpA were expressed and purified from
223 *E. coli* (Supp Figure S1), and then subjected to analytical ultracentrifugation
224 (AUC). The sedimentation coefficient distribution of RNase J indicates that this
225 protein forms two oligomeric species *in vitro* with concentration-independent
226 sedimentation coefficients (S_0) of 5.8 and 8.8. These two species were
227 compatible with a monomer and a dimer, which was confirmed by calculation of
228 the theoretical sedimentation coefficients with the HYDROPRO software. Based
229 on the structural data of *H. pylori* RNase J presented above, the calculation of
230 the sedimentation coefficient was 5.4 and 8.9 for a monomer and dimer
231 respectively. On the other hand, the calculated sedimentation for the dimer is fully
232 compatible with the extended arrangement of the C-terminal end, showing that
233 dimerization locks the structure in an extended conformation. Therefore, we
234 concluded that the two forms of RNase J observed by AUC are indeed a
235 monomer and a dimer (Figure 2A) that have a structural arrangement in solution
236 which is compatible with the observed crystal structure. The monomeric
237 population predominates (~60%) over the dimer (~40%) independently of the
238 protein concentration, showing that these species were not under equilibrium but
239 were dependent on other modifications.

240 AUC of RhpA shows behavior as a monomer independent of concentration
241 with an S_0 of 3.85 (Figure 2B).
242

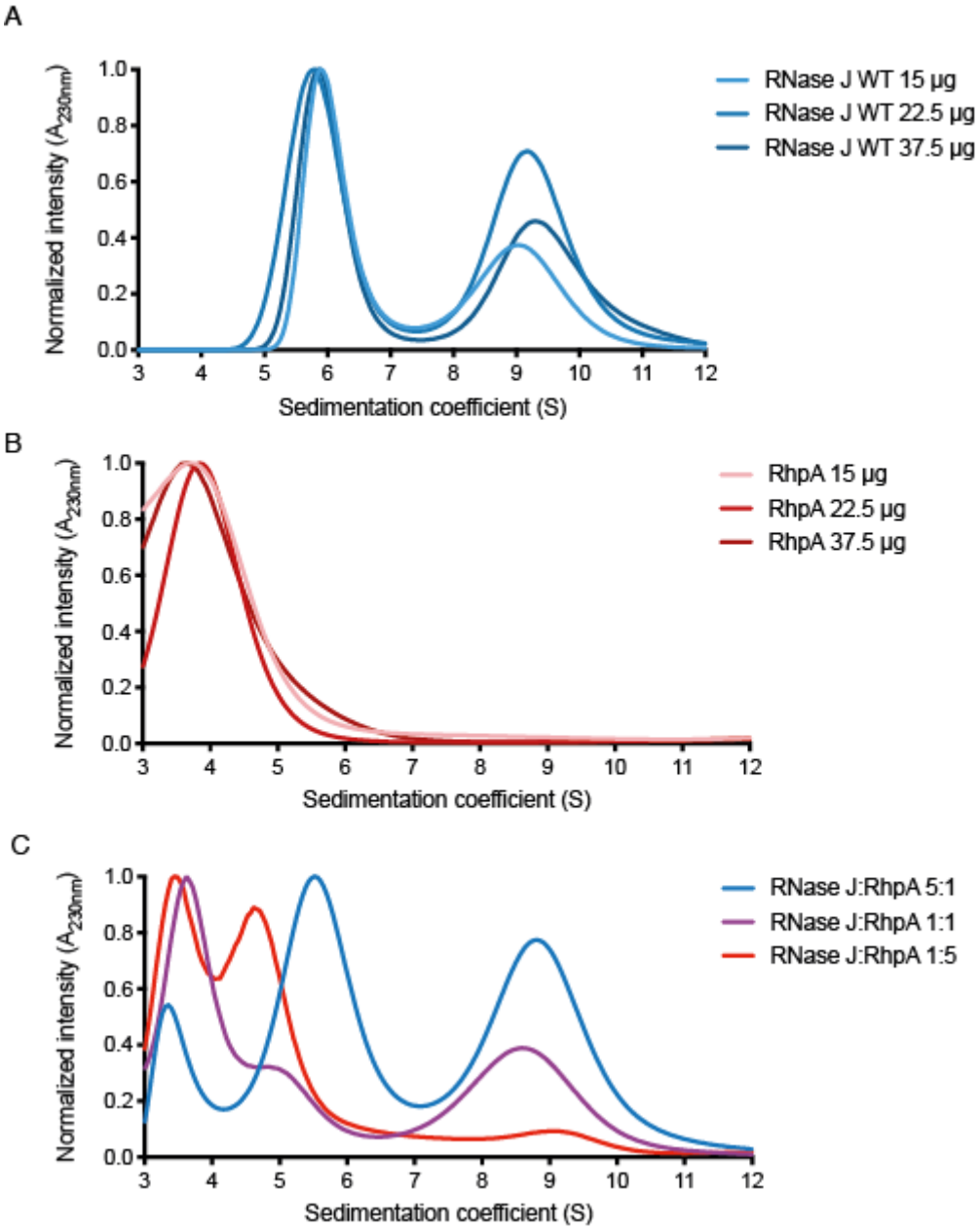

243
244 **Figure 2. The solution oligomerization state of RNase J, RhpA and the degradosome**
245 **assembly.** The profiles are from analytical ultracentrifugation sedimentation of (A) RNase J, (B)
246 RhpA and (C) the degradosome complex at different ratios of RNase J and RhpA. The profiles
247 were recorded at 230 nm wavelength.
248
249
250 **RNase J and RhpA form a 1:1 minimal degradosome complex**

251 Next, we wanted to evaluate the stoichiometry of the protein complex formed
252 by RNase J and RhpA. We mixed both proteins at 5:1, 1:1 and 1:5 ratios and
253 subjected them to AUC (Figure 2C). When using a 5:1 RNase J:RhpA ratio, we
254 identified three peaks corresponding to both proteins alone (RNase J monomer
255 and dimer and RhpA monomer). With a 1:1 RNase J:RhpA ratio, three peaks
256 could be detected. Based on the previous calculations, these peaks are proposed
257 to correspond to (i) RhpA monomer alone for the 3.85S peak, (ii) a dimer of
258 RNase J for the 8.8S peak, and (iii) a minor peak with a sedimentation coefficient
259 of 4.8S that would correspond to the RNase J-RhpA complex. This latter peak
260 was much more prominent when using a 1:5 ratio of RNase J:RhpA, where only
261 two peaks could be detected, corresponding to RhpA alone and most probably
262 the complex with a coefficient of 4.8S. From this peak and the available frictional
263 coefficients, we calculated a mass for the complex of approximately 124 kDa that
264 is only compatible with a complex with a 1:1 stoichiometry. Interestingly, neither
265 the monomer nor the dimer of RNase J was detected under this condition, and
266 all RNase J was involved in complex formation. We thus conclude that RNase J
267 and RhpA form a 1:1 stoichiometry complex *in vitro*.
268
269 **Bacterial two hybrid (BACTH) to identify residues important for the**
270 **oligomerization of RNase J**
271 As AUC results show that oligomerization is not controlled by kinetics, we then
272 searched for the potential residues involved in the self-interaction of RNase J
273 using bacterial two hybrid (BACTH) experiments that test the interaction of
274 protein pairs in *E. coli*. First, a consistent interaction of wild type RNase J with
275 itself was detected (Figure 3A). Then, different RNase J mutants were
276 constructed and tested. As previously reported for other RNase J proteins (Zhao
277 et al., 2015), we found that the C-terminal region of RNase J is essential for this
278 interaction. Next, in order to pinpoint residues that are important for RNase J
279 multimerization, we constructed RNase J mutants in which nine charged residues
280 of this C-terminal domain were individually replaced by alanine residues. As
281 shown in Figure 3A, several mutants were significantly affected in their capacity
282 to homo-oligomerize, including RNase J E618A, E654A, K660A, E663A and
283 K649A. These data show that charged residues at the C-terminal domain of
284 RNase J are important for its self-interaction.

285 These residues are not at the predicted dimerization interface of the C-terminal
286 domain, but they are likely to be involved in stabilizing the domain through
287 interactions with side chains of complementary charge.
288

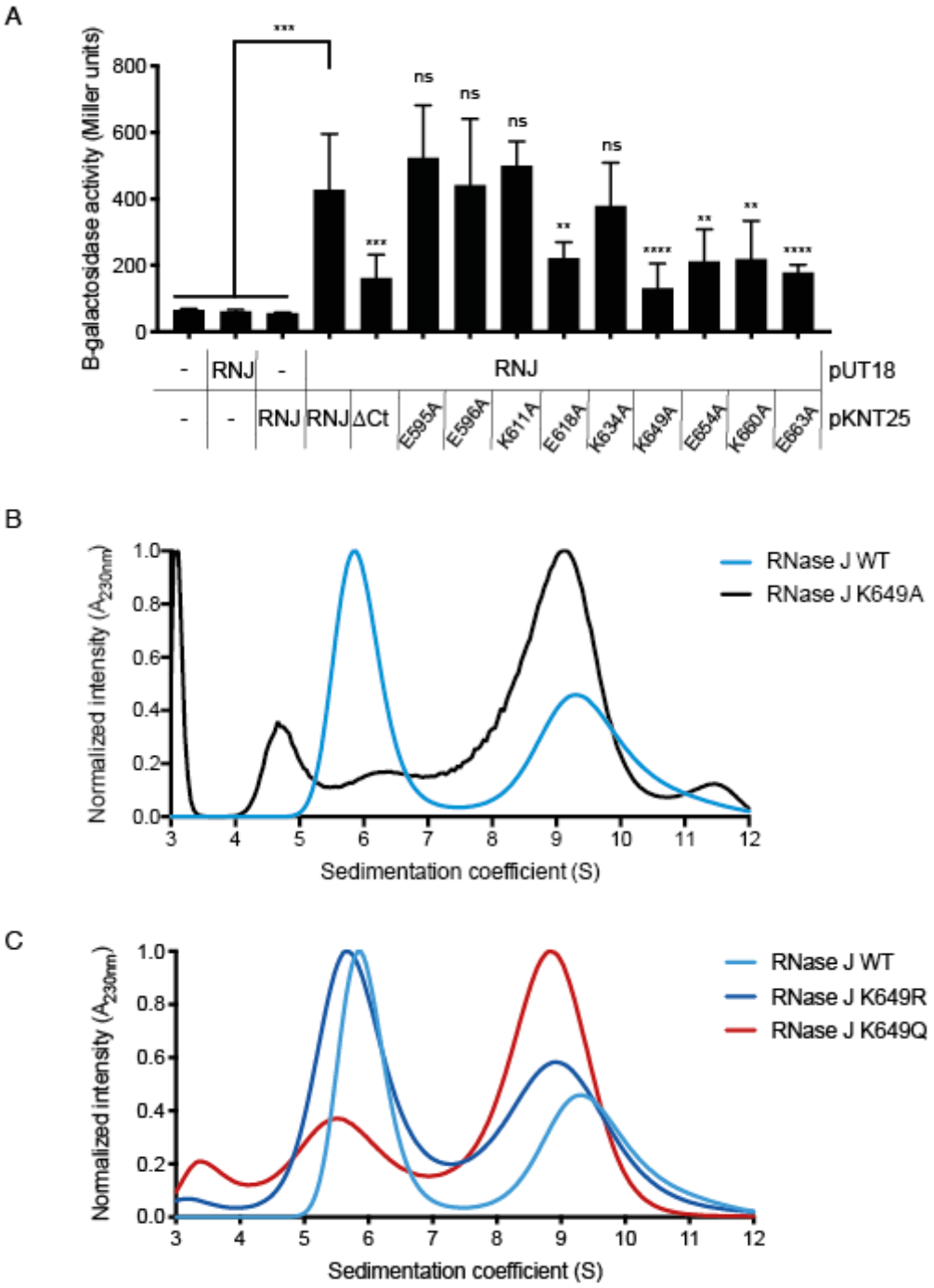

289
290 **Figure 3**. **Point mutations modify the oligomeric state of RNase J.** (A) BACTH two hybrid
291 experiments to asses homo-oligomerization of WT and mutant RNase J proteins. Differences in
292 the beta-galactosidase activity units are indicated with ns (non-significant) ** p-value<0.005, ***
293 p-value<0.0005, **** p-value<0.0001. (B) Analytical ultracentrifugation sedimentation profiles of
294 RNase J WT and variant K649A at 230 nm wavelength. (C) Analytical ultracentrifugation

295 sedimentation profiles of RNase J WT and variants K649R and K649Q at 230 nm wavelength.
296
297
298 **RNase J is acetylated at several lysine residues**
299 RNase R and RNase II from *E. coli* have been reported to be post-
300 translationally modified by acetylation but no such modification was reported on
301 RNase J. A mass spectrometry (MS) analysis was performed on an RNase J-
302 FLAG fusion protein expressed from the *H. pylori* chromosome (Supp Figure S1)
303 under the control of its native promoter. The RNase J-FLAG protein was pulled
304 down from crude lysates using anti-FLAG antibodies and extracted from a
305 polyacrylamide gel. The experiment was performed on three biological replicates
306 from cultures in exponential phase. We found that nine lysine residues of RNase
307 J, spread across all protein domains, are consistently acetylated: K134, K140,
308 K323, K337, K397, K511, K547, K634 and K649 (Supp Figure S2 and Supp Table
309 S2).
310
311 **Lysine 649 is important for the oligomerization state of RNase J**
312 Lysine 649 (K649), localized at the RNase J C-terminal domain, was
313 particularly interesting since this residue was both acetylated and required for
314 RNase J homo-oligomerization in two hybrid experiments. Therefore, AUC
315 analyses were performed with purified RNase J variants (Supp Figure S1) to test
316 the importance of K649 in RNase J homo-oligomerization. As shown in Figure
317 3B, the purified RNase J K649A mutant assembles exclusively as a dimer *in vitro*,
318 with a complete loss of the monomeric population seen with the WT protein.
319 Circular dichroism was performed to verify that this effect was not due to a defect
320 in the folding of RNase J K649A. The circular dichroism spectra of wild-type and
321 K649A variants of RNase J did not show significant differences (Supp Figure S3)
322 and the estimated proportions of the different secondary structure elements were
323 maintained (Supp Table S3). This shows that mutation K649A does not introduce
324 a major folding defect in RNase J secondary structure. Thus, K649 is important
325 for RNase J dimerization both *in vitro* and in *E. coli*.
326
327 **Acetylation mimicry of Lysine 649 affects the oligomeric state of RNase J**

328 Given that K649 is acetylated, we next investigated whether RNase J
329 acetylation at this residue could represent a control level of its oligomeric state.
330 Therefore, we constructed an RNase J mutant in which K649 was either replaced
331 by an arginine residue (K649R), that mimics a non-acetylated state but maintains
332 a positive charge at this position, or replaced by a glutamine residue (K649Q)
333 which mimics an acetylated state while neutralizing the positive charge [a
334 previously validated strategy (Kamieniarz and Schneider, 2009)]. As shown in
335 Figure 3C, the AUC sedimentation profile of RNase J K649R is similar to that of
336 the wild type enzyme. In contrast, RNase J K649Q shows a significantly
337 increased proportion of dimers over the monomers, similarly to the K649A mutant
338 (Figure 3B-C). These data show that the positive charge of K649 is important for
339 the stability of the RNase J monomer and that oligomerization is controlled by the
340 charge state of K649.
341
342 **Mutations in K649 alter the exoribonuclease activity of RNase J**
343 Since RNase J WT forms both monomers and dimers *in vitro*, we next
344 assessed whether the oligomeric state and the presence of a charge at position
345 649 were correlated with differences in the *in vitro* activity of this protein. The
346 exoribonuclease activity of RNase J was measured with a 24-nt long single
347 stranded RNA substrate from the 5'-untranslated region (UTR) of *rnj*, upon which
348 we previously found RNase J to be active (Redko et al., 2016). This substrate
349 was labeled with 6-carboxyfluorescein (6FAM) at either the 3' or 5'-ends. As a
350 control, a mutant inactivated at the RNase J active site, D299A, was constructed.
351 We found, as expected, that the D299A inactive mutant did not degrade the
352 substrate while the wild type RNase J was active in its 5'-3' exoribonucleolytic
353 mode (Figure 4A-B). This activity is evident from the rapid depletion in the intact
354 substrate bands labelled in 5' (Figure 4A) or 3' (Figure 4B) and, from the
355 additional accumulation of the 1nt product upon digestion of the 5'-labeled
356 substrate (Figure 4A).
357 The RNase J mutant with K649 replaced by R, that mimics a non-acetylated
358 state, and which behaves as monomers and dimers like the WT protein, was
359 strongly affected in its exoribonuclease activity (Figure 4).
360 In contrast, the protein variants with K649 replaced either by A (that abolishes
361 both the positive charge at this position and the acetylation) or by Q (acetylation-

362 mimicking mutation) and that both mainly assembled into dimers, presented an
363 activity that was significantly higher than that of the RNase J K649R variant. The
364 half-lives of the substrates were calculated from three independent experiments
365 for the wild type and for every RNase J variant and are shown in Table 1.
366 From these data, we conclude that, for these mutants, the dimeric form of
367 RNase J is most probably the active form *in vitro*. Altogether, we identified a
368 residue, K649, whose charge is important for RNase J activity and
369 oligomerization and that is acetylated in *H. pylori* cells. This indicates a
370 mechanism of control of RNase J activity that is based on the allosteric control of
371 its dimerization by acetylation.
372

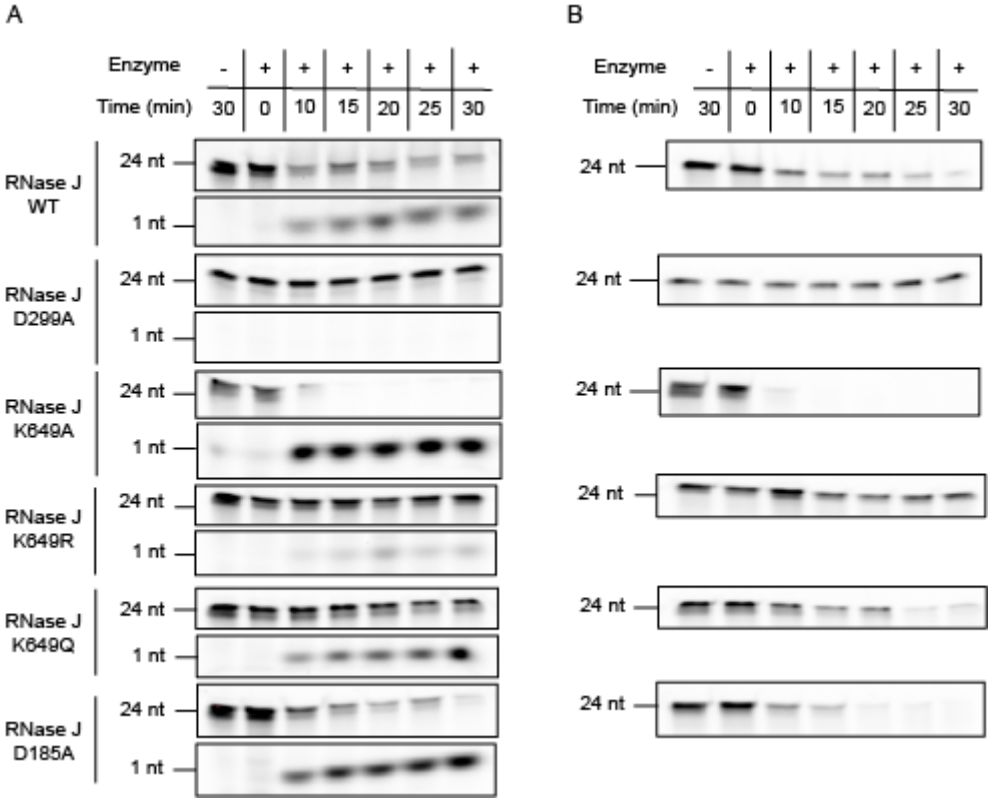

373
374 **Figure 4. Exoribonuclease activity of RNase J wild type and mutants**. (A) Exoribonuclease
375 activity of RNase J WT and different variants using a 24-nt RNA substrate labeled with 6-
376 carboxyfluorescein (6-FAM) at its 5'-end over the course of 30 min. (B) Exoribonuclease activity
377 of RNase J WT and different variants using a 24-nt RNA substrate labeled with 6-FAM at its 3'-
378 end over the course of 30 min.
379
380
381 **Table 1**. Half-lives of fluorescent RNA substrates in the presence of wild type RNase J and
382 different variants either alone or in complex with RhpA.

	Half-life ± SD (min)			
RNase J variant	5'-labeled substrate (exo)	3'-labeled substrate (exo)	3'-labeled substrate (endo)	3'-labeled substrate + RhpA (complex)
WT	18.77 ± 3.16	7.37 ± 3.36	31.36 ± 17.57	6.29 ± 2.92
D299A	>30 [165.04 ± 93.36]	>>>30	>75 [231.05 ± 163.38]	n.d.
K649A	4.52 ± 0.52	2.75 ± 0.82	10.3 ± 0.56	6.95 ± 0.49
K649R	>30 [222.80 ± 175.05]	>30 [36.61 ± 12.04]	>75 [81.83 ± 6.81]	27.70 ± 5.4
K649Q	>30 [56.80 ± 13.02]	14.82 ± 9.11	>75 [92.52 ± 26.85]	37.33 ± 28.89
D185A	9.14 ± 4.83	4.56 ± 1.15	28.6 ± 9.67	n.d.

The activity of the RNase J-RhpA complex is not affected by K649 mutations

Next, we wanted to determine whether mutations of K649 affect the activity of the RNase J-RhpA complex. For this, we used a 45-nt long RNA substrate with hairpin structures at both ends to prevent the exoribonuclease activity from the 5'-extremity and labeled it with 6FAM at the 3' end [as in (17), Supp Figure S4A]. First, the activity of RNase J WT and mutant proteins alone was tested on this substrate. As compared to the linear substrate, the degradation kinetics of this substrate by RNase J was significantly reduced but not abolished, suggesting that RNase J might attack this substrate by its endoribonuclease activity and then proceeds by exoribonuclease activity. As we previously reported, in a functional degradosome complex, RhpA will unwind the secondary structure elements and allow RNase J to act in its exoribonucleolytic mode. Most interestingly, the activity tests with a mixture of RNase J and RhpA in a 1:1 ratio resulted in a significant decrease in the half-life of the substrate to 6.3±2.9 min as compared to the activity of RNase J alone (approx. 31.4±17.6 min), compatible with a functional complex (Table 1). The half-life of the structured substrate incubated with the complex between RhpA and the RNase J K649A variant (that has increased exoribonuclease activity) was not affected (half-life 6.7±0.5 min) (Supp Figure S4B and Table 1). We conclude that the activity of the RNase J-RhpA complex is not significantly affected by the K649A mutation.

Residue D185 is important for oligomeric state and the activity of RNase J

407 The RNase J structure suggests that residue D185 may indirectly support
408 dimerization. The residue is in an interaction network that supports a helical
409 extension involving residues 584-594 that supports interactions with the C-
410 terminal domain. In agreement with our predictions, the AUC analysis of the
411 RNase J D185A mutant revealed a much smaller proportion of the monomer, with
412 a predominating dimeric population, as compared to the wild type protein (Figure
413 5). Consistently with what we found for mutant K649A, this was correlated with
414 higher exoribonucleolytic activity of RNase J D185A (Figure 4A-B and Table 1),
415 suggesting again that the structural destabilization of the monomer leads to an
416 increased amount of dimer with an enhanced enzymatic activity.
417

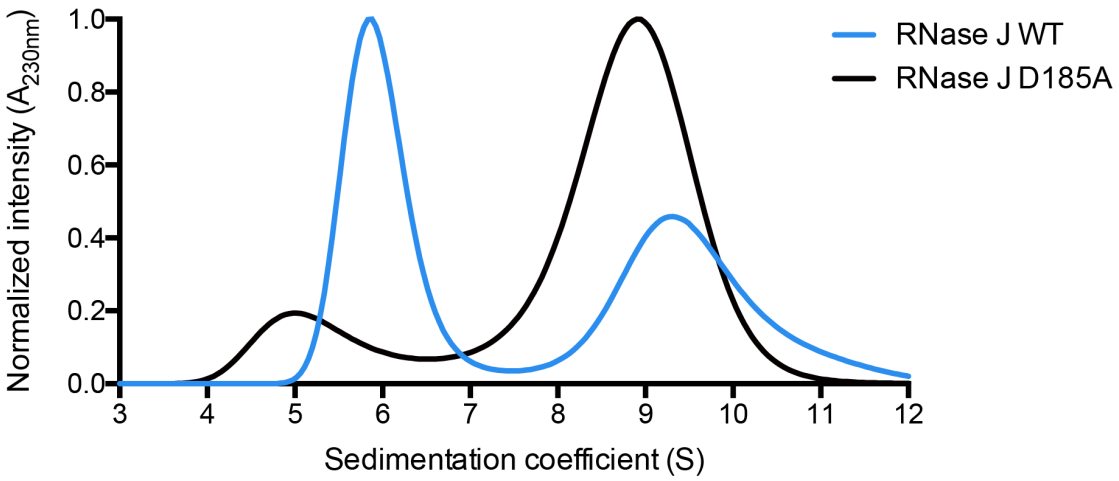

418
419 **Figure 5. Impact of D185A mutation on RNase J oligomeric state.** Analytical
420 ultracentrifugation sedimentation profiles of RNase J WT and variant D185A, recorded at 230 nm
421 wavelength.
422
423
424 **Analysis of the consequences of RNase J mutations on *H. pylori***
425 **morphology**
426 We next wanted to examine the consequences of the mutations affecting
427 RNase J oligomerization and/or acetylation state in live *H. pylori* cells. Since
428 RNase J is an essential protein, strains carrying mutations in the acetylated
429 residues identified above were constructed with the following strategy. *H. pylori*
430 strain B128 was transformed with plasmid pILL2157 derivatives either expressing
431 wild type or mutant variants of RNase J under the control of an IPTG-inducible
432 promoter. Then, the chromosomal wild type copy of RNase J was deleted by

433 homologous recombination and replacement with a kanamycin resistance
434 cassette.
435 In *B. subtilis*, mutants deficient in RNase J1 present an altered cell morphology
436 (Figaro et al., 2013). Therefore, the morphology of our *H. pylori* RNase J mutant
437 strains was examined by phase contrast microscopy and quantified with the
438 MicrobeJ software (Ducret et al., 2016). The wild type B128 strain presents cells
439 that are relatively heterogeneous in shape and with an average length of
440 2.15±0.67 µm. We observed that, in a strain expressing wild type RNase J from
441 the system described above, the *H. pylori* cells were longer in the absence of
442 IPTG [lower amount of RNase J as compared to the WT strain (Redko et al.,
443 2016)], than upon induction with 1 mM IPTG (where the expression of RNase J
444 is induced), 2.44±0.61 µm vs. 2.05±0.51 µm, respectively (Figure 6). This
445 indicates that in *H. pylori*, RNase J is also regulating a factor required to maintain
446 wild type cell morphology. Interestingly, we noted that the observed phenotype is
447 not dependent on the activity of RNase J alone but rather on the RNA
448 degradosome complex, as IPTG induction of RNase J WT in a strain lacking
449 RhpA fails to complement this phenotype (average length of 3.41±0.83 µm)
450 (Figure 6A).
451 When we performed these tests with strains that expressed different RNase J
452 variants, we identified two groups of mutations. In the first group, the RNase J
453 variants behaved similarly to the wild type enzyme, as their expression upon
454 IPTG addition resulted in a reduction of bacterial length. This was the case for
455 RNase J K323A, K547A and K649A and, to a lesser extent, RNase J K634A. In
456 the second group, that includes variants K134A, K140A, K337A, K397A and
457 K511A, the strains presented a strong growth defect and substantial cell lysis and
458 cellular debris were observed. In these cases, the cells were short with a
459 tendency towards a coccoid morphology that is typical of *H. pylori* cultures under
460 stress (El Mortaji et al., 2020). This phenotype was particularly evident in the case
461 of cells expressing variant K397A. For these cultures, addition of IPTG favored
462 bacterial growth but failed to restore the typical helical form of healthy *H. pylori*
463 cells, suggesting that RNase J function is strongly impaired.

464 These results show that RNase J activity is important for the correct regulation
465 of growth and cell morphology in *H. pylori* and that several of the residues that
466 we found to be acetylated are important for RNase J function.

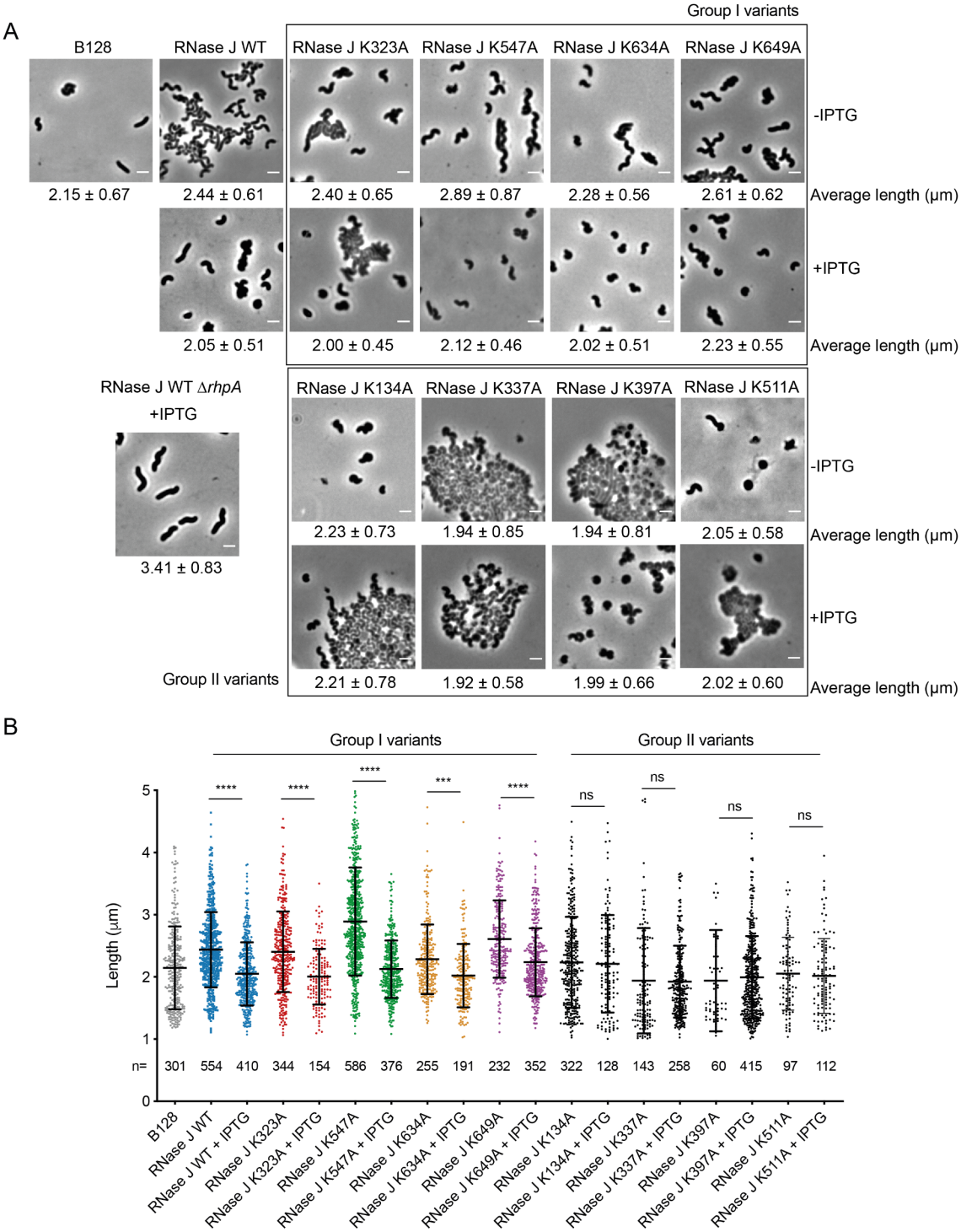

467

468 **Figure 6**. *Helicobacter pylori* cell morphology is affected by RNase J abundance and point
469 mutations at lysine residues that are acetylation targets. (A) Phase contrast microscopy images
470 of *H. pylori* Δ*rnj* B128 strains expressing WT or mutant versions of RNase J from plasmid
471 pILL2157 without (top panels) or with IPTG induction (bottom panels). The phenotype of a *H.*
472 *pylori* Δ*rnj*-Δ*rhpA* strains expressing WT RNase J from a plasmid is also shown. The scale bar

473 represents 2 μm. (B) Dot plots showing the distribution of the cell lengths of wild type and the
474 different mutants without or with IPTG. Horizontal lines indicate the mean length and the error
475 bars are the standard deviation. ns (non-significant), ***p-value<0.0005, ****p-value<0.0001.
476

477 **RNase J is acetylated through a range of mechanisms in *H. pylori***

478 Several pathways contribute to acetylation in bacteria (Christensen et al.,
479 2019a). We tried to elucidate which are the enzymes responsible for the different
480 acetylation events that occur on the RNase J of *H. pylori*. Therefore, we used the
481 *H. pylori* strain expressing an RNase J-FLAG fusion from the chromosome to
482 introduce deletions in genes that we predicted as acetylase candidates. The
483 RNase J-FLAG protein was enriched from these strains and analyzed by MS as
484 explained above. The tests were performed from three biological replicates. The
485 acetylase candidate genes were *hpb8_615* [henceforth referred to as *rimI*, as it
486 presents homology to *rimI* from *E. coli* (Christensen et al., 2018)] and *hpb8_1270*
487 [that contains two Gcn5-acetyltransferase (GNAT) domains]. Non-enzymatic
488 acetylation by acetyl-CoA and acetyl-phosphate also occurs in bacteria
489 (Christensen et al., 2019b, 2019a). The impact of this pathway was assessed in
490 *H. pylori* by constructing a mutant in the *pta-ackA* operon that is in charge of
491 acetyl-phosphate synthesis and metabolism. As shown in Figure 7, we found that
492 several pathways influence the acetylation of RNase J lysine residues. RimI is
493 partially responsible for the acetylation of RNase J residues K323, K397 and
494 K649. The HPB8_1270 protein is partially responsible for the acetylation of
495 residues K323, K397, K511 and K649. Acetyl phosphate-mediated non-
496 enzymatic acetylation participated in the acetylation of K134, K323, K397 and
497 K511 and K649. For other residues, namely K140, K337, K547 and K634, no
498 change in acetylation levels was detected in the mutants, suggesting that other
499 acetylation mechanisms are likely at play in *H. pylori*. These results suggest a
500 high redundancy of the different acetylation mechanisms that act on RNase J,
501 particularly on residues K323, K397 and K649.

502 Thus, multiple mechanisms participate in the acetylation of RNase J on
503 different residues.

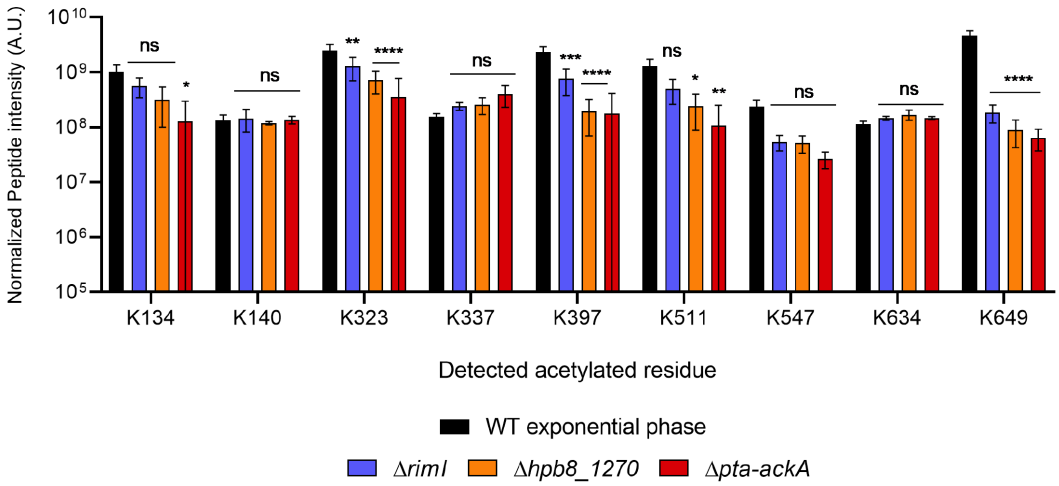

Figure 7. RNase J peptides containing acetylated residues. The normalized intensities were obtained by mass spectrometry from strains expressing FLAG-tagged RNase J in a wild-type background or in a mutant strain lacking different acetylation mechanism. ns (non-significant) p-value>0.05, *p-value<0.05, **p-value<0.005, ***p-value<0.0005, ****p-value<0.0001. Error bars represent the standard deviation.

512 **Discussion**

513 In this study, we defined the structure of the major *H. pylori* ribonuclease
514 RNase J and its *in vitro* oligomerization state alone and in the RNA degradosome
515 with its RhpA RNA helicase partner. We also identify *in vivo* acetylation patterns
516 of RNase J and demonstrate that these impact on oligomerization and activity *in*
517 *vitro* and *in vivo*.

518 We found, by AUC, that RNase J is in equilibrium between monomeric and
519 dimeric states. Earlier studies showed that *D. radiodurans* RNase J also is
520 distributed between monomers and dimers (Zhao et al., 2015). *Bsu*RNase J1
521 forms dimers and tetramers *in vitro* (Newman et al., 2011) and, when mixed with
522 *Bsu*RNase J2, heterotetramers (Mathy et al., 2010). Similarly, RNase J1 from *S.*
523 *aureus* forms homodimers and homotetramers *in vitro* (Hausmann et al., 2017b).
524 RNase J of *S. pyogenes* crystalizes as tetramers that are composed of a dimer-
525 of-dimers (Pei et al., 2015). In the present study, at the studied *H. pylori* RNase
526 J concentrations, no trace of tetramerization could be seen by AUC. It is likely
527 that the observed tetrameric structure in the X-ray structure is due to crystal
528 packaging and that it does not reflect the arrangement of RNase J in solution, as
529 the dimer seems to be the active form. In addition, RhpA alone behaves as a
530 monomer in solution by AUC. Together, RNase J and RhpA form a complex that
531 is compatible with a 1:1 stoichiometry.

532 Acetylation has emerged in recent years as a major post-translational
533 regulatory mechanism in prokaryotes (Carabetta and Cristea, 2017), and a few
534 examples of its influence in RNases and RNA-degrading enzymes have been
535 described, including *E. coli* RNase R (Liang et al., 2011) and RNase II (Song et
536 al., 2016) and *B. subtilis* CshA (Ogura and Asai, 2016). Here, we found that, in
537 *H. pylori*, as many as 9 lysine residues of RNase J were consistently acetylated,
538 although probably not at the same time, which constitutes the first evidence of
539 protein acetylation in *H. pylori*. One of these residues is K649, which we also
540 found to be involved in the oligomerization state of RNase J by BACTH in *E. coli*.
541 Interestingly, this residue is located at the C-terminal domain of RNase J (Supp
542 Figure S2). This region was also shown to be important for the oligomerization
543 and exoribonucleolytic activity of the RNase J of *D. radiodurans* (Zhao et al.,
544 2015). Therefore, we examined the role of K649 in RNase J oligomerization (by
545 AUC) and exoribonuclease activity. Three mutants were analyzed, RNase J

546 K649A that abolishes the side chain of the lysine residue, K649R that mimics a
547 non-acetylated state while maintaining the positive charge and K649Q that
548 mimics an acetylated state (Kamieniarz and Schneider, 2009). Whereas the
549 K649R variant maintains a sedimentation profile similar to that of the wild type
550 enzyme, variants lacking a positive charge in K649, either K649Q or K649A, had
551 an increased proportion of dimer or displayed no monomeric form, respectively.
552 Interestingly, we observed that the K649R variant is less active than the wild type
553 RNase J whereas variants K649Q and K649A are more active than the K649R
554 variant.

555 Our model indicated that residue K649 is not located at the interaction surface
556 between the subunits of the dimer, but that it rather plays a structural role in the
557 integrity of the overall structure. We conclude that elimination of the positive
558 charge at residue 649 leads to a higher stabilization of the dimeric species. In
559 agreement with this hypothesis, we observed that D185A, another mutation in a
560 structurally important residue, had the same effect and favors the dimeric
561 species. Interestingly, in *D. radiodurans*, the corresponding residue (D61) had
562 already been identified as key for RNase J dimerization (Zhao et al., 2015).
563 Electrostatic interactions of charged side chains on the surface of proteins can
564 strongly contribute to the fold stability (Perutz, 1978; Perutz and Raidt, 1975;
565 Zhou and Pang, 2018). We propose that the network of surface electrostatic
566 interactions stabilizes the CTD of RNase J, which in turn supports the homodimer.
567 The CTD is the primary self-complementary interface of the dimer, and the
568 interface between the core (amino acids 137-586) and between the dimer-of-
569 dimers formed by the core both have marginal stability in isolation. Thus,
570 changes in the charge, through acetylation, can thereby impact on stability of the
571 CTD fold and oligomerization state.

572 The question naturally arises of how the catalytic activity of RNase J is affected
573 by its oligomerization state. A clue is suggested in the overlay of the structure of
574 *H. pylori* RNase J with the *S. coelicolor* homologue, in which there is a bound
575 RNA substrate engaged at the active site (Pei et al., 2015) (Figure 1D). There
576 are marked differences in the positions of loops at the entrance to the catalytic
577 site that would obstruct the RNA from following the same route in the *H. pylori*
578 enzyme, but the nucleic acid could approach the site from the opposite rim of the
579 entrance. The exposed peptide loop regions are positioned to accommodate the

580 CTD. It is possible that changes in the oligomerization state, through changes in
581 CTD stability, will impact on the presentation of those loops and access to the
582 active site in a gating mechanism.

583 Altogether, our results suggest that mutations that favor the dimeric RNase J
584 conformation also increase the activity of RNase J of *H. pylori in vitro*. As the
585 charge of residue 649 is important for dimerization, acetylation of K649 might tilt
586 the balance of the RNase J species towards the dimeric form and potentially
587 increase its activity. In this way, acetylation on K649 can modulate the activity of
588 RNase J in *H. pylori* cells. Formation of the RNase J-RhpA complex is not
589 affected by mutations or modifications of residue K649 in the ribonuclease, and
590 thus such mutations do not significantly alter the activity of this complex. Earlier
591 studies indicate that RNase J and the RNase J-RhpA complex can act on different
592 transcripts (Redko et al., 2013, 2016; Tejada-Arranz et al., 2021). It can be
593 envisaged that acetylation of K649 would therefore have a differential impact on
594 the subset of free RNase J that is not part of a degradosome assembly.

595 Furthermore, we addressed the role of the acetylated residues that we
596 identified in *H. pylori* cells. It has been described that *B. subtilis* cells lacking
597 RNase J1 show morphology defects with a tendency to filament (Figaro et al.,
598 2013). We thus evaluated the morphology of *H. pylori* cells expressing RNase J
599 variants, in which each acetylated lysine was replaced by an alanine residue. We
600 observed that cells with a reduced concentration of wild type RNase J are longer
601 than those in which RNase J expression is induced. This revealed that RNase J,
602 most probably indirectly, is involved in the control of *H. pylori* length. Interestingly,
603 this phenotype does not depend on the activity of RNase J alone, but rather on
604 the RNA degradosome complex, since the overexpression of RNase J WT in a
605 Δ*rhpA* strain does not reduce cell length. Given that we previously showed that
606 about 80% of *H. pylori* mRNAs are at least two times more abundant in an RNase
607 J-depleted mutant, it is difficult to define the target mRNA that is causing the
608 observed elongation phenotype (Redko et al., 2016). One possibility would be
609 the overexpression of MreC (9.3-fold upregulated in an RNase J-depleted strain),
610 that has been shown to cause cell filamentation in *H. pylori* (El Ghachi et al.,
611 2011).

612 Alanine replacement of the different acetylated positions of RNase J leads to
613 different phenotypes, showing that acetylation is indeed important for RNase J

614 activity in *H. pylori*. Variant K649A behaves like the wild type enzyme in this test,
615 in agreement with the notion that the morphology phenotype depends on the
616 activity of the whole RNA degradosome complex, which is not affected by
617 whether there is a charge in this position or not. The phenotype of the K134A
618 mutant suggests that it is affected in RNase J activity; interestingly this residue is
619 located within the N-terminal extension of *Hp*RNase J (Supp Figure S2), that we
620 previously found to be very important for efficient RNase J activity (Redko et al.,
621 2016). However, it is not known how these acetylated residues impact RNase J
622 properties. They could affect its stability, activity, oligomerization, degradosome
623 complex formation, compartmentalization, binding of other partners or RNA, or a
624 combination of these.

625 We found that several mechanisms participate in the acetylation of the different
626 residues of RNase J. Our results indicate that HPB8_1270 and the *H. pylori* RimI
627 homologue indeed function as acetylases. In addition, we uncovered a role of
628 non-enzymatic acetylation by acetyl phosphate that is produced and metabolized
629 by the Pta and AckA enzymes. The *E. coli* RimI protein is a multifunctional
630 acetyltransferase, that can perform ε-lysine acetylation and Nα acetylation on the
631 L31 and S18 ribosomal proteins, respectively (Christensen et al., 2018; Isono and
632 Isono, 1980), with high substrate specificity. In contrast, RimI from
633 *Mycobacterium tuberculosis* is an Nα acetylase with more relaxed substrate
634 specificity *in vitro* (Pathak et al., 2016). Here, we found that the *H. pylori* RimI
635 targets K323, K397 and K649 of RNase J. HPB8_1270 is a protein belonging to
636 the DUF2156 family, containing two GNAT domains. It presents homology with
637 the BT_3689 protein from *Bacteroides thetaiotaomicron*, which contains an
638 acetyl-CoA molecule in its active site (PDB 2HQY), suggesting its function as an
639 acetyltransferase. Here, we found that HPB8_1270 is involved in the acetylation
640 of K323, K397, K511 and K649, showing that in *H. pylori* this protein is most likely
641 an acetyltransferase. Lastly, acetyl phosphate-mediated acetylation, which is
642 responsible for most acetylation events in *E. coli* and *B. subtilis* (Christensen et
643 al., 2019b, 2019a), was important for the acetylation of K134, K323, K397, K511
644 and K649.

645 These data demonstrate that multiple mechanisms can target the same lysine
646 residue and that there is a high redundancy in the functions of these acetylation
647 mechanisms. Acetylation at residue K649 was strongly dependent on three such

648 mechanisms; this redundancy could testify of a critical importance of acetylation
649 at this position. In addition, other acetylation mechanisms could occur in *H. pylori*
650 that might account for some of these acetylation events. More work is needed, in
651 particular using multiple mutants to determine how many of these mechanisms
652 can target the different residues and the influence of the different acetylation
653 mechanisms on the activity and regulation of RNase J and the RNA
654 degradosome.

655 Using Clustal Omega 1.2.4 (Sievers et al., 2011), we performed an alignment
656 of the RNase J proteins of *H. pylori* and of the closely related organism
657 *Campylobacter jejuni*, but also of the more distant *B. subtilis*, *S. aureus*, *S.*
658 *pyogenes* and *D. radiodurans*. Interestingly, this revealed that most of the
659 acetylated lysines are conserved in *H. pylori* and *C. jejuni* RNase J proteins, and
660 some of them are also conserved in more distant organisms (Supp Figure S5).
661 The case of K511 is particularly interesting, as it is conserved in *S. pyogenes*, *B.*
662 *subtilis*, *H. pylori* and *C. jejuni*, and in the case of *S. aureus* this position is a Q
663 residue which might behave as a “permanently-acetylated” lysine. In *H. pylori*,
664 the mutant expressing RNase J K511A variant presents a strong growth defect.
665 The relevance of lysine acetylation in the regulation of the activity of the RNases
666 J from other organisms remains to be addressed.

667 In conclusion, we have established that RNase J is acetylated on multiple
668 lysine residues through different mechanisms, and that its acetylated residues
669 affect the activity of RNase J and phenotypes such as cell morphology.
670 Furthermore, our data suggests that acetylation on K649 can influence the
671 oligomeric state and activity of RNase J, and that the dimeric form could be the
672 most active one. Thus, acetylation is an important player in the modulation of the
673 activity of RNase J and of the RNA degradosome of *H. pylori*.
674

675 **Materials and methods**

676 *Bacterial strains and growth conditions*

677 The bacterial strains used in this study are summarized in Supp Table S4. *H.*
678 *pylori* strains were derivatives of strain B128 (Farnbacher et al., 2010; McClain et
679 al., 2009). Plasmids (Supp Table S4) were constructed and amplified using *E.*
680 *coli* XL1-Blue (Agilent Technologies). *H. pylori* strains were grown on Blood agar
681 base 2 (Oxoid) plates supplemented with 10% defibrinated horse blood and with
682 an antibiotic-antifungal cocktail composed of 2.5 µg/mL amphotericin B, 0.31
683 µg/mL polymyxin B, 6.25 µg/mL trimethoprim and 12.5 µg/mL vancomycin. *H.*
684 *pylori* mutants were selected using 20 µg/mL kanamycin, 10 µg/mL apramycin or
685 6 µg/mL chloramphenicol. For liquid cultures, we used Brucella broth
686 supplemented with 10% fetal calf serum (FCS) (Eurobio), the antibiotic-antifungal
687 cocktail and, when necessary, chloramphenicol to select for plasmid-containing
688 bacteria. *H. pylori* cells were grown at 37ºC under a microaerophilic atmosphere
689 (6% O_2, 10% CO_2, 84% N_2) using an Anoxomat (Mart Microbiology) atmosphere
690 generator.

691

692 *Plasmid preparation and transformations*

693 A NucleoBond Xtra midi kit (Macherey-Nagel) and a QIAamp DNA minikit
694 (Qiagen) were used for plasmid preparations for *H. pylori* transformation and
695 genomic DNA extractions, respectively. For plasmid preparations for *E. coli*
696 transformation and sequencing, a QIAprep Spin Miniprep kit (Qiagen) was used.
697 PCR was carried out with either DreamTaq DNA polymerase (Thermofisher) or
698 with Q5 High-Fidelity DNA polymerase (NEB) when the product required a high-
699 fidelity polymerase. A list of the oligonucleotides that were used can be found in
700 Supp Table S5.

701

702 *Construction of H. pylori mutants and fusions*

703 The cassette for the construction of the *H. pylori* RNase J-FLAG strain was
704 constructed by the isothermal assembly technique (Gibson et al., 2009), by
705 assembling in frame the last 500 bp of the *rnj* gene followed by the FLAG-tag, the
706 apramycin resistance gene and the 500 bp immediately downstream from *rnj*.
707 The resulting fragment was PCR-amplified and 1 µg of the product was
708 introduced into *H. pylori* by natural transformation. Transformants were selected

709 on plates with apramycin. Strains carrying the pILL2157 plasmid carrying wild
710 type *rnj* gene (Redko et al., 2013) and its derivates with the different *rnj* mutants
711 (constructed following standard procedures with the primers compiled in Supp
712 Table S5) were transformed in the same manner with 1.5 µg of the plasmids and
713 selected in plates with chloramphenicol. The resulting strains were then used to
714 transform by cassettes constructed in a similar manner to delete the *rnj* gene and
715 replace it by a kanamycin resistance gene [as in (Redko et al., 2013)]. The
716 transformants were selected on plates containing kanamycin, chloramphenicol
717 and 1 mM IPTG to allow the expression of the copy of *rnj* from the plasmid.
718 Plasmids for BACTH were constructed from plasmids pUT18 and pKNT25
719 (Karimova et al., 1998) by inserting wild type or mutant variants of the *rnj* gene in
720 the *Pst*I and *Kpn*I restriction sites following standard techniques using plasmids
721 indicated in Supp Table S4.
722 Deletion of the genes of interest, construction of fusions and/or insertion of
723 cassettes was verified by PCR and sequencing of the region of interest.
724
725 *Purification and crystallography of RNase J*
726 A vector co-expressing residues 21-465 of RhpA with a C-terminal 3C-HALP-
727 his6 tag and residues 139-691 of RNase J (C1hRSEj) (from strain 26695 gene
728 HP1430, UniProt P56185) with a C-terminal hexa-histidine tag was generated by
729 the Oxford Protein Production Facility at Harwell. Cells were grown in terrific broth
730 supplemented with 0.5 M NaCl and 1 mM betain, 30 µg/mL kanamycin, 50 µg/mL
731 carbenicillin and 20 µg/mL chloramphenicol. Cells were grown at 37°C until
732 optical density at 600 nm reached 0.3, then moved to 20°C and induced with 0.2
733 mM IPTG (isopropyl β-D-1-thiogalactopyranoside) for 24 hours. Cells were
734 harvested by centrifugation, then suspended in 50 mM Tris pH 7.4, 50 mM
735 HEPES (4-(2-hydroxyethyl)-1-piperazineethanesulfonic acid) pH 7.4, 500 mM
736 NaCl, 1 mM TCEP (tris(2-carboxyethyl)phosphine), 0.05% v/v Triton X-100, 5%
737 v/v glycerol and 10 mM imidazole and stored frozen. The suspension was
738 thawed, passed 5 times through a cell disruptor (Avestin Emulsiflex C5
739 homogeniser, 1000 bars) and clarified by centrifugation at 37000 g for 30
740 minutes, 5°C. The supernatant was applied to a HiTrap Ni chelating column,
741 washed with lysis buffer containing 0.01% v/v Triton X-100, and 15 mM imidazole,
742 then eluted with a gradient in imidazole. The optimal fractions were pooled and

743 cleaved with 3CP-GST protease cleavage, using 300 µl of 0.85 mg/mL protease
744 to cleave C1/RSE protein isolated from 1 L culture, at 4ºC overnight. This step
745 removes HALO-Chis-tag on RhpA. The 3CP-cleaved protein was loaded onto
746 HALO-RESIN and the flow-through collected, which contained the RNase
747 J/helicase complex. The sample was concentrated with a 30kD MWCO
748 centrifugal concentrator and applied to a S200 SEC column equilibrated in 20
749 mM Tris-HCl pH 7.4, 20 mM HEPES pH 7.4, 150 mM NaCl, 5% glycerol, 0.1%
750 v/v Triton X-100, 1 mm TCEP. The sample was concentrated with a 30kD MWCO
751 centrifugal concentrator to optical density at 280 nm of 3.38 and used in
752 crystallization screens. Crystals were found in PEG I screen 0.1 M HEPES pH
753 7.5, 25% wt/v polyethylene glycol 1000.
754 Diffraction data were collected at I24 at Diamond Light source at wavelength
755 0.9778 Å using a Pilatus6M detector. Crystals are in space group P4122 with cell
756 dimensions a=b=158 c=214.26 Å. The structure was solved by molecular
757 replacement *Streptomyces* RNase J (PDB 3BK2) with PHASER and the CCP4
758 suite (McCoy et al., 2007; Winn et al., 2011). There was no space in the lattice
759 for the RhpA protein. The model of RNase J 139-691 was built using COOT
760 (Emsley et al., 2010) and refined with PHENIX (Afonine et al., 2012). A homology
761 model for the C-terminal domain, residues 587 to 691, was prepared using
762 PHYRE2 (Kelley et al., 2015), and the structure of the full-length protein was
763 predicted using the ROBETTA server (Baek et al., 2021). The C-terminal domain
764 from the ROBETTA model was docked into the map and fitted as a rigid body
765 and then linked to the model of the well resolved core (139-586). As the density
766 for the C-terminal domain was poorly resolved due to disorder, the side chains
767 were removed. A final cycle of refinement using the core only (137-586) and not
768 the disordered C-terminal domain were used to provide the refinement
769 parameters summarized in the supplementary Table S1. A monomer of RNase J
770 139-691 occupies the asymmetric unit, and the tetramer is generated through
771 crystallographic symmetry. Estimates of buried surface area were made using
772 the PISA program in the CCP4 suite (Krissinel and Henrick, 2007). The model
773 and structure factors have been deposited in the PDB with accession code 7PCR.
774
775
776 *Beta-galactosidase assays*

777 Bacterial two hybrid assays were carried out in *E. coli* strain BTH101 as
778 previously described (Karimova et al., 1998). Briefly, strains carrying derivatives
779 of the two vectors, pUT18 and pKNT25, were grown overnight in 1 mL LB with
780 40 µg/mL kanamycin, 100 µg/mL ampicillin and 0.1 mM IPTG. The OD at 600 nm
781 of the resulting cultures was measured in a TECAN plate reader and the beta-
782 galactosidase activity was calculated by mixing 500 µL of the cultures with 500
783 µL of buffer Z, 100 µL of chloramphenicol and 50 µL of 0.1% SDS, vortexing the
784 cells and then adding 200 µL of 4 mg/mL ONPG. The reactions were incubated
785 at 28ºC until they turned yellow and the reactions were stopped by adding 500
786 µL of 1 M Na_2CO_3. Samples were centrifuged for 5 min at 14,000 rpm and the
787 OD at 420 and 550 nm of the upper fraction was measured in a TECAN plate
788 reader. The beta-galactosidase activity (Miller units) was calculated as described
789 (Miller, 1972).
790
791 *Protein expression and purification*
792 Wild type and variant versions of RNase J and RhpA were cloned into a
793 pET28a+ vector in *E. coli* XL1-Blue and then transformed in *E. coli* Bli5 for
794 expression. The strains were grown in 800 mL cultures in LB with 40 µg/mL
795 kanamycin and 25 µg/mL chloramphenicol and, once they reached an OD of 0.5-
796 0.8, were induced with 1 mM IPTG. The cultures were incubated at 30ºC and 160
797 rpm during 3 h. The cells were collected by centrifugation at 4000 rpm in an Avanti
798 J-E centrifuge (Beckman Coulter) with a JA-14 rotor at 4ºC during 30 min and
799 pellets were frozen at -80ºC until further processing.
800 Pellets were thawed on ice and resuspended on lysis buffer containing 25 mM
801 Tris-HCl pH 7.8 for RNase J and pH 8 for RhpA, 500 mM NaCl, 10% glycerol, 20
802 mM imidazole, 1 mM dithiothreitol (DTT), 50 U benzonase and protease inhibitor
803 cocktail (c0mplete EDTA-free, Roche). Cells were lysed by sonication and
804 centrifuged for 30 min at 4000 rpm in a 5810R centrifuge (Eppendorf) at 4ºC to
805 eliminate cellular debris. The supernatant was then incubated overnight at 4ºC
806 and under agitation with 2 mL Ni-NTA resin (50% v/v, Thermofisher) pre-
807 equilibrated with lysis buffer.
808 Resins were packed onto Poly-Prep Chromatography columns (Bio-Rad) and
809 washed with 10 volumes of 25 mM Tris-HCl at the appropriate pH, 300 mM NaCl,
810 1 mM DTT and 20 mM imidazole, 10 volumes of the same buffer with 50 mM

811 imidazole and 10 volumes of the same buffer with 100 mM imidazole. The elution
812 was carried out with an elution buffer containing 25 mM Tris-HCl at the
813 appropriate pH, 300 mM NaCl, 1 mM DTT and 500 mM imidazole, in 1 mL
814 fractions. Aliquots of the resulting fractions were run on a 4-20% Mini-Protean
815 TGX stain-free precast protein gel (Bio-Rad) at 200V for 30 min and stained by
816 Imperial protein stain (ThermoFisher). After destaining, the corresponding purest
817 fractions were chosen, mixed and concentrated using Vivaspin 20 tubes (MWCO
818 30,000 Da, GE Healthcare) down to 1 mL volumes. The buffer was replaced using
819 G-25 columns (PD MidiTrap G-25, GE Healthcare) with 25 mM Tris-HCl, 300 mM
820 NaCl, 1 mM DTT and 10% glycerol. Samples were aliquoted and frozen at -80ºC.
821
822 *Analytical ultracentrifugation*
823 Samples of purified proteins were thawed on ice and the buffer was replaced
824 using G-25 columns (PD MiniTrap G-25, GE Healthcare) with 25 mM Tris-HCl pH
825 8, 300 mM NaCl and 0.5 mM Tris(2-carboxyethyl)phosphine (TCEP, Sigma).
826 Appropriate amounts of the different proteins were mixed and diluted in the same
827 buffer with a final volume of 300 µL that was charged into 2 sector analytical
828 ultracentrifugation cells. The concentration of the proteins was 3 mM when there
829 was only one protein, 3 mM:3 mM when two proteins were in equimolar amounts
830 and 1 mM:5 mM when the proteins were mixed at a 1:5 ratio. The centrifugation
831 was performed for 16 h on an Optima analytical ultracentrifuge (Beckman-
832 Coulter) with an 8-hole AnTi50 rotor, at 42,000 rpm and 20ºC, measuring the
833 optical density at 230 nm in order to determine the sedimentation profile of the
834 protein or complex. The data was analyzed with the Sedfit software (NIH) using
835 a diffusion deconvoluted continuous sedimentation coefficient distribution c(s)
836 with one discrete component model (Schuck, 2000). The model was chosen in
837 order to take in consideration the signal due to TCEP absorption. The presented
838 graphs correspond to a resolution of 300 points with a confidence interval of 0.9.
839 For the individual proteins, the sedimentation coefficient independent of the
840 concentration (S_0) was calculated.
841 The partial specific volume ($\overline{\nu}$) of the proteins was estimated by the software
842 Sednterp (Laue et al., 1992) based on the amino acid sequence. This software
843 was also used for the calculation of the density and viscosity of the buffer used

844 throughout the experiments. Calculation of sedimentation coefficients for protein
845 structures was performed with the program Hydropro (Ortega et al., 2011).
846
847 *Circular dichroism*
848 The near-UV absorption spectra (195-260 nm) were measured, in the same
849 buffer as for the AUC experiments, by circular dichroism with a Circular Dichroism
850 Spectrometer Model 215 (Aviv instruments) using 0.2 mm optical path cells with
851 5 mM of RNase J WT and K649A mutant. The proportions of the different
852 secondary structure elements were determined with the BeStSel software
853 (Micsonai et al., 2015, 2018) based on the amino acid sequence.
854
855 *Ribonuclease activity tests*
856 The endoribonuclease and exoribonuclease activities were measured using 6-
857 carboxyfluorescein (6FAM)-labeled RNA substrates either in 5' or in 3' as listed
858 in Supp Table S5. 500 nM RNA substrate were incubated with 500 nM protein in
859 a total volume of 10 µL with a buffer containing 50 mM Tris-HCl pH 7.8, 100 mM
860 NaCl, 8 mM $MgCl_2$, 0.1 mM and 0.1 mg/mL bovine serum albumin (BSA). The
861 reactions were carried out at 37ºC for 0-30 min for the exoribonuclease activity
862 tests and 0-75 min for endoribonuclease activity tests. Reactions were stopped
863 by adding 98% formamide and 10 mM ethylene diamine tetraacetic acid (EDTA)
864 and by incubating for 15 min at 95 ºC.
865 The degradation products were run on a Mini-Protean TBE-Urea gels (Bio-
866 Rad) that was pre-run for 60 min at 200 V. The samples were run for 5 min at 50
867 V and then for 30 min at 200 V. Gels were visualized on a Chemidoc MP Imaging
868 System (Bio-Rad) with 0.2 s exposure at 488 nm. The gels were then stained
869 with ethidium bromide to reveal the molecular weight marker (ssRNA molecular
870 weight marker, Takara). Experiments were performed in triplicate and images
871 were quantified ImageLab (Bio-Rad, version 6.1). Decay coefficients, λ, were
872 calculated with the formula $N(t) = N_0 e^{-\lambda t}$, where *N(t)* is the amount of substrate
873 at time *t* and N_0 is the initial amount. The half-lives, $t_{1/2}$ were then calculated with
874 the formula $t_{1/2} = \frac{Ln(2)}{\lambda}$.
875
876 *Phase contrast microscopy*

877 Phase contrast microscopy was performed with an Axio Observer microscope
878 (Zeiss) equipped with an Axiocam camera with X100 magnification. Image
879 acquisition was performed with the axiovision software. Images were cropped
880 and adjusted using FiJi software. The length of wild type cells and that of cells
881 expressing wild type or mutant versions of RNase J from a plasmid, with or
882 without 1 mM IPTG, was measured by using the MicrobeJ plugin of ImageJ
883 (Ducret et al., 2016) with the following parameters: cell area above 0.7 μm^2,
884 minimal length of 1 µm and cell width between 0.4-1 µm.
885
886 *Pulldown and mass spectrometry*
887 *H. pylori* cultures of strains expressing FLAG-tagged RNase J were grown in
888 15 mL of Brucella medium until an $OD_{600\ nm}$ of 0.6-1.2 for exponential phase
889 cultures. Cells were pelleted by centrifugation for 10 min at 4 ºC and 4000 rpm
890 and resuspended in PBS to an $OD_{600\ nm}$ of 10. Cells were lysed by sonication and
891 cell debris were eliminated by centrifugation for 10 min at 13000 rpm and 4 ºC.
892 The supernatant constitutes the total extract fraction.
893 Pulldowns were performed using 2 µL of monoclonal anti-FLAG M2 antibodies
894 produced in mice (F3165, Sigma) per reaction and 50 µL of magnetic protein G-
895 coated Dynabeads according to the supplier's instructions (Dynabeads Protein G
896 for Immunoprecipitation, 10003D, ThermoFisher). Proteins were eluted in the
897 denaturing mode and run in a 4-20% Mini-Protean TGX stain-free precast protein
898 gel (Bio-Rad) at 200V for 30 min and stained by Imperial protein stain
899 (ThermoFisher) and destained.
900 Each band corresponding to RNase J-FLAG was cut and washed several
901 times in 50 mM ammonium bicarbonate (ABC)-acetonitrile (ACN) (1:1) for 15 min
902 at 37 °C. Disulfide bonds were reduced with 10 mM DTT and cysteines alkylated
903 with 55 mM chloroacetamide. Trypsin (V5111, Promega) digestion was
904 performed overnight at 37 °C in 50 mM ABC. Peptides were extracted from the
905 gel by two incubations in 50 mM ABC-ACN-formic acid (FA) (50:50:0.5) for 15
906 min at 37 °C. After ACN evaporation in a Speed-Vac, resulting peptides were
907 desalted with stage-tip (Rappsilber et al., 2007) using C18 Empore disc and
908 eluted with 80% ACN, 0.1% FA. Peptides were resuspended in 2% ACN, 0.1%
909 FA prior to liquid chromatography coupled to mass spectrometry (LC-MS/MS)
910 analysis.

911 For LC-MS/MS, a nanochromatographic system (Proxeon EASY-nLC 1200 -
912 ThermoFisher Scientific) was coupled on-line to a Q Exactive™ Plus Mass
913 Spectrometer (ThermoFisher Scientific) using an integrated column oven (PRSO-
914 V1 - Sonation GmbH, Biberach, Germany). For each sample, peptides were
915 loaded on an in-house packed 26 cm nano-HPLC column (75 µm inner diameter)
916 with C18 resin (1.9 µm particles, 100 Å pore size, Reprosil-Pur Basic C18-HD
917 resin, Dr. Maisch GmbH, Ammerbuch-Entringen, Germany) after an equilibration
918 step in 100 % solvent A (H_2O, 0.1% FA).
919 Peptides were eluted with a multi-step gradient using 2 to 7 % solvent B (80%
920 ACN, 0.1% FA) during 5 min, 7 to 23% during 70 min, 23 to 45% during 30 min
921 and 45 to 95% during 5 min at a flow rate of 300 nL/min over 132 min. Column
922 temperature was set to 60°C.
923 MS data were acquired using Xcalibur software using a data-dependent Top
924 10 method with a survey scans (300-1700 m/z) at a resolution of 70,000 and a
925 MS/MS scans (fixed first mass 100 m/z) at a resolution of 17,500. The AGC target
926 and maximum injection time for the survey scans and the MS/MS scans were set
927 to 3E6, 20 ms and 1E6, 60 ms respectively. The isolation window was set to 1.6
928 m/z and normalized collision energy fixed to 28 for HCD fragmentation. We used
929 a minimum AGC target of 1E4 for an intensity threshold of 1.7E5. Unassigned
930 precursor ion charge states as well as 1, 7, 8 and >8 charged states were rejected
931 and peptide match was disable. Exclude isotopes was enabled and selected ions
932 were dynamically excluded for 30 seconds.
933 Raw data were analyzed using MaxQuant software version 1.6.6.0 (Tyanova
934 et al., 2016) using the Andromeda search engine (Cox et al., 2011). The MS/MS
935 spectra were searched against a UniProt *Helicobacter pylori* [strain B8
936 (Farnbacher et al., 2010; McClain et al., 2009)] database (download in
937 24/06/2019, 1,719 entries) and tagged RNase J. Usual known mass spectrometry
938 contaminants and reversed sequences of all entries were included.
939 Andromeda searches were performed choosing trypsin as specific enzyme
940 with a maximum number of five missed cleavages. Possible modifications
941 included carbamidomethylation (Cys, fixed), oxidation (Met, variable), Nter
942 acetylation (variable) and K acetylation (Lys, variable) for in-gel peptides. The
943 mass tolerance in MS was set to 20 ppm for the first search then 4.5 ppm for the

944 main search and 20 ppm for the MS/MS. Maximum peptide charge was set to
945 seven and five amino acids were required as minimum peptide length.
946 A false discovery rate (FDR) cutoff of 1 % was applied at the peptide and
947 protein levels.
948 Raw files and MaxQuant files (msms.txt) were processed in Skyline-daily
949 20.1.9.268 (MacLean et al., 2010) to generate MS1-XIC and perform peak
950 integration for each K-acetylated peptide. Normalization across samples was
951 performed by using the mean of the ratios from non-modified peptides (Supp
952 Table S2).
953 The mass spectrometry data have been deposited to the
954 ProteomeXchange Consortium via de PRIDE partner repository (Perez-Riverol
955 et al., 2019) with the dataset identifier PXD027670.
956
957 *Statistical analyses*
958 Statistical analysis was performed using Prism 9. We applied one-way
959 ANOVA with Dunnett's multiple comparisons test in Figure 2A, one-way ANOVA
960 with Sidak's multiple comparisons test in Figure 6B and two-way ANOVA with
961 Dunnett's multiple comparisons test in Figure 7.
962
963

964 **Acknowledgements**

965 We would like to thank Sébastien Brûlé and Bruno Baron for their help with
966 AUC and circular dichroism experiments, and Frédéric Fischer for bioinformatical
967 analysis regarding protein HPB8_1270. We thank Diane Soussan and Yulia
968 Redko for their help in preliminary experiments of this project. ATA is part of the
969 Pasteur - Paris University (PPU) International PhD Program. This project has
970 received funding from the European Union's Horizon 2020 research and
971 innovation program under the Marie Sklodowska-Curie grant agreement Nº
972 665807, and from the Institut Carnot Pasteur Microbes & Santé. MBL was a
973 master student of the UTC (Université de Technologie de Compiègne). Support
974 was provided by "Fondation pour la Recherche Médicale" for the grant
975 DBF20161136767 to HDR and the Pasteur-Weizmann Consortium of “The Roles
976 of Noncoding RNAs in Regulation of Microbial Life Styles and Virulence” to HDR.
977 BFL and XYP are supported by a Wellcome Trust Investigator award
978 (200873/Z/16/Z). The authors would like to thank the DIM 1HEALTH region Ile-
979 de-France for funding the Centrifection project that has allowed the Optima
980 ultracentrifuge investment. We thank the staff of the OPPL at Harwell Campus,
981 UK for preparing vectors, screening expression conditions for the recombinant
982 proteins, and helpful discussions.

983

984 **References**

985 Afonine, P. V, Grosse-Kunstleve, R.W., Echols, N., Headd, J.J., Moriarty, N.W.,
986 Mustyakimov, M., Terwilliger, T.C., Urzhumtsev, A., Zwart, P.H., and Adams,
987 P.D. (2012). Towards automated crystallographic structure refinement with
988 phenix.refine. Acta Crystallogr. D. Biol. Crystallogr. *68*, 352–367.
989 Amieva, M., and Peek, R.M. (2016). Pathobiology of Helicobacter pylori–
990 Induced Gastric Cancer. Gastroenterology *150*, 64–78.
991 Baek, M., DiMaio, F., Anishchenko, I., Dauparas, J., Ovchinnikov, S., Lee, G.R.,
992 Wang, J., Cong, Q., Kinch, L.N., Schaeffer, R.D., et al. (2021). Accurate
993 prediction of protein structures and interactions using a three-track neural
994 network. Science.
995 Boneca, I.G., Ecobichon, C., Chaput, C., Mathieu, A., Guadagnini, S., Prévost,
996 M.-C., Colland, F., Labigne, A., and de Reuse, H. (2008). Development of
997 inducible systems to engineer conditional mutants of essential genes of
998 Helicobacter pylori. Appl. Environ. Microbiol. *74*, 2095–2102.
999 Callebaut, I., Moshous, D., Mornon, J.P., and De Villartay, J.P. (2002). Metallo-
1000 β-lactamase fold within nucleic acids processing enzymes: The β-CASP family.
1001 Nucleic Acids Res. *30*, 3592–3601.
1002 Carabetta, V.J., and Cristea, I.M. (2017). Regulation, Function, and Detection of
1003 Protein Acetylation in Bacteria. J. Bacteriol. *199*, e00107-17.
1004 Christensen, D.G., Meyer, J.G., Baumgartner, J.T., D'Souza, A.K., Nelson,
1005 W.C., Payne, S.H., Kuhn, M.L., Schilling, B., and Wolfe, A.J. (2018).
1006 Identification of Novel Protein Lysine Acetyltransferases in Escherichia coli.
1007 MBio *9*, e01905-18.
1008 Christensen, D.G., Xie, X., Basisty, N., Byrnes, J., McSweeney, S., Schilling, B.,
1009 and Wolfe, A.J. (2019a). Post-translational Protein Acetylation: An Elegant
1010 Mechanism for Bacteria to Dynamically Regulate Metabolic Functions. Front.
1011 Microbiol. *10*, 1604.
1012 Christensen, D.G., Baumgartner, J.T., Xie, X., Jew, K.M., Basisty, N., Schilling,
1013 B., Kuhn, M.L., and Wolfe, A.J. (2019b). Mechanisms, Detection, and
1014 Relevance of Protein Acetylation in Prokaryotes. MBio *10*, 02708–02718.
1015 Cox, J., Neuhauser, N., Michalski, A., Scheltema, R.A., Olsen, J. V, and Mann,
1016 M. (2011). Andromeda: a peptide search engine integrated into the MaxQuant
1017 environment. J. Proteome Res. *10*, 1794–1805.

1018 Ducret, A., Quardokus, E.M., and Brun, Y. V. (2016). MicrobeJ, a tool for high
1019 throughput bacterial cell detection and quantitative analysis. Nat. Microbiol. *1*,
1020 16077.
1021 Eisenbart, S.K., Alzheimer, M., Pernitzsch, S.R., Dietrich, S., Stahl, S., and
1022 Sharma, C.M. (2020). A Repeat-Associated Small RNA Controls the Major
1023 Virulence Factors of Helicobacter pylori. Mol. Cell.
1024 Emsley, P., Lohkamp, B., Scott, W.G., and Cowtan, K. (2010). Features and
1025 development of Coot. Acta Crystallogr. D. Biol. Crystallogr. *66*, 486–501.
1026 Farnbacher, M., Jahns, T., Willrodt, D., Daniel, R., Haas, R., Goesmann, A.,
1027 Kurtz, S., and Rieder, G. (2010). Sequencing, annotation, and comparative
1028 genome analysis of the gerbil-adapted Helicobacter pylori strain B8. BMC
1029 Genomics *11*, 335.
1030 Figaro, S., Durand, S., Gilet, L., Cayet, N., Sachse, M., and Condon, C. (2013).
1031 Bacillus subtilis mutants with knockouts of the genes encoding ribonucleases
1032 RNase Y and RNase J1 are viable, with major defects in cell morphology,
1033 sporulation, and competence. J. Bacteriol. *195*, 2340–2348.
1034 El Ghachi, M., Matteï, P.-J., Ecobichon, C., Martins, A., Hoos, S., Schmitt, C.,
1035 Colland, F., Ebel, C., Prévost, M.-C., Gabel, F., et al. (2011). Characterization of
1036 the elongasome core PBP2 : MreC complex of Helicobacter pylori. Mol.
1037 Microbiol. *82*, 68–86.
1038 Gibson, D.G., Young, L., Chuang, R.-Y., Venter, J.C., Hutchison, C.A., and
1039 Smith, H.O. (2009). Enzymatic assembly of DNA molecules up to several
1040 hundred kilobases. Nat. Methods *6*, 343–345.
1041 Hausmann, S., Guimarães, V.A., Garcin, D., Baumann, N., Linder, P., and
1042 Redder, P. (2017a). Both exo- and endo-nucleolytic activities of RNase J1 from
1043 *Staphylococcus aureus* are manganese dependent and active on
1044 triphosphorylated 5′-ends. RNA Biol. *14*, 1431–1443.
1045 Hausmann, S., Guimarães, V.A., Garcin, D., Baumann, N., Linder, P., and
1046 Redder, P. (2017b). Both exo- and endo-nucleolytic activities of RNase J1 from
1047 *Staphylococcus aureus* are manganese dependent and active on
1048 triphosphorylated 5′-ends. RNA Biol. *14*, 1431–1443.
1049 Isono, K., and Isono, S. (1980). Ribosomal protein modification in Escherichia
1050 coli. II. Studies of a mutant lacking the N-terminal acetylation of protein S18.
1051 Mol. Gen. Genet. *177*, 645–651.

1052 Kamieniarz, K., and Schneider, R. (2009). Tools to Tackle Protein Acetylation.
1053 Chem. Biol. *16*, 1027–1029.
1054 Karimova, G., Pidoux, J., Ullmann, A., and Ladant, D. (1998). A bacterial two-
1055 hybrid system based on a reconstituted signal transduction pathway. Proc. Natl.
1056 Acad. Sci. U. S. A. *95*, 5752–5756.
1057 Kelley, L.A., Mezulis, S., Yates, C.M., Wass, M.N., and Sternberg, M.J.E.
1058 (2015). The Phyre2 web portal for protein modeling, prediction and analysis.
1059 Nat. Protoc. *10*, 845–858.
1060 Krissinel, E., and Henrick, K. (2007). Inference of Macromolecular Assemblies
1061 from Crystalline State. J. Mol. Biol. *372*, 774–797.
1062 Laue, T., Shah, B., Ridgeway, T., and Pelletier, S. (1992). Computer-aided
1063 interpretation of analytical sedimentation data for proteins. In Analytical
1064 Ultracentrifugation in Biochemistry and Polymer Science, S.E. Harding, A.
1065 Rowe, and J. Horton, eds. (Cambridge: Royal Society of Chemistry), pp. 90–
1066 125.
1067 Liang, W., Malhotra, A., and Deutscher, M.P. (2011). Acetylation Regulates the
1068 Stability of a Bacterial Protein: Growth Stage-Dependent Modification of RNase
1069 R. Mol. Cell *44*, 160–166.
1070 MacLean, B., Tomazela, D.M., Shulman, N., Chambers, M., Finney, G.L.,
1071 Frewen, B., Kern, R., Tabb, D.L., Liebler, D.C., and MacCoss, M.J. (2010).
1072 Skyline: an open source document editor for creating and analyzing targeted
1073 proteomics experiments. Bioinformatics *26*, 966–968.
1074 Mathy, N., Hébert, A., Mervelet, P., Bénard, L., Dorléans, A., Li de la Sierra-
1075 Gallay, I., Noirot, P., Putzer, H., and Condon, C. (2010). *Bacillus subtilis*
1076 ribonucleases J1 and J2 form a complex with altered enzyme behaviour. Mol.
1077 Microbiol. *75*, 489–498.
1078 McClain, M.S., Shaffer, C.L., Israel, D.A., Peek, R.M., and Cover, T.L. (2009).
1079 Genome sequence analysis of Helicobacter pylori strains associated with
1080 gastric ulceration and gastric cancer. BMC Genomics *10*, 3.
1081 McCoy, A.J., Grosse-Kunstleve, R.W., Adams, P.D., Winn, M.D., Storoni, L.C.,
1082 Read, R.J., and IUCr (2007). Phaser crystallographic software. J. Appl.
1083 Crystallogr. *40*, 658–674.
1084 Micsonai, A., Wien, F., Kernya, L., Lee, Y.-H., Goto, Y., Réfrégiers, M., and
1085 Kardos, J. (2015). Accurate secondary structure prediction and fold recognition

1086 for circular dichroism spectroscopy. Proc. Natl. Acad. Sci. U. S. A. *112*, E3095-
1087 103.
1088 Micsonai, A., Wien, F., Bulyáki, É., Kun, J., Moussong, É., Lee, Y.-H., Goto, Y.,
1089 Réfrégiers, M., and Kardos, J. (2018). BeStSel: a web server for accurate
1090 protein secondary structure prediction and fold recognition from the circular
1091 dichroism spectra. Nucleic Acids Res. *46*, W315–W322.
1092 Miller, J.H. (1972). Experiments in molecular genetics (Cold Spring Harbor
1093 Laboratory).
1094 El Mortaji, L., Aubert, S., Galtier, E., Schmitt, C., Anger, K., Redko, Y., Quentin,
1095 Y., and De Reuse, H. (2018). The sole DEAD-box RNA helicase of the gastric
1096 pathogen Helicobacter pylori is essential for colonization. MBio *9*, e02071-17.
1097 El Mortaji, L., Tejada-Arranz, A., Rifflet, A., Boneca, I.G., Pehau-Arnaudet, G.,
1098 Radicella, J.P., Marsin, S., and De Reuse, H. (2020). A peptide of a type I toxin-
1099 antitoxin system induces Helicobacter pylori morphological transformation from
1100 spiral shape to coccoids. Proc. Natl. Acad. Sci. U. S. A.
1101 Newman, J.A., Hewitt, L., Rodrigues, C., Solovyova, A., Harwood, C.R., and
1102 Lewis, R.J. (2011). Unusual, Dual Endo- and Exonuclease Activity in the
1103 Degradosome Explained by Crystal Structure Analysis of RNase J1. Structure
1104 *19*, 1241–1251.
1105 Nooren, I.M.A., and Thornton, J.M. (2003). Diversity of protein-protein
1106 interactions. EMBO J. *22*, 3486–3492.
1107 Ogura, M., and Asai, K. (2016). Glucose Induces ECF Sigma Factor Genes,
1108 sigX and sigM, Independent of Cognate Anti-sigma Factors through Acetylation
1109 of CshA in Bacillus subtilis. Front. Microbiol. *7*, 1918.
1110 Ortega, A., Amorós, D., and García de la Torre, J. (2011). Prediction of
1111 hydrodynamic and other solution properties of rigid proteins from atomic- and
1112 residue-level models. Biophys. J. *101*, 892–898.
1113 Pathak, D., Bhat, A.H., Sapehia, V., Rai, J., and Rao, A. (2016). Biochemical
1114 evidence for relaxed substrate specificity of Nα-acetyltransferase
1115 (Rv3420c/rimI) of Mycobacterium tuberculosis. Sci. Rep. *6*, 28892.
1116 Pei, X.-Y., Bralley, P., Jones, G.H., and Luisi, B.F. (2015). Linkage of catalysis
1117 and 5' end recognition in ribonuclease RNase J. Nucleic Acids Res. *43*, 8066–
1118 8076.
1119 Perez-Riverol, Y., Csordas, A., Bai, J., Bernal-Llinares, M., Hewapathirana, S.,

1120 Kundu, D.J., Inuganti, A., Griss, J., Mayer, G., Eisenacher, M., et al. (2019). The
1121 PRIDE database and related tools and resources in 2019: improving support for
1122 quantification data. Nucleic Acids Res. *47*, D442–D450.
1123 Perutz, M.F. (1978). Electrostatic effects in proteins. Science (80-.). *201*, 1187–
1124 1191.
1125 Perutz, M.F., and Raidt, H. (1975). Stereochemical basis of heat stability in
1126 bacterial ferredoxins and in haemoglobin A2. Nature *255*, 256–259.
1127 Rappsilber, J., Mann, M., and Ishihama, Y. (2007). Protocol for micro-
1128 purification, enrichment, pre-fractionation and storage of peptides for
1129 proteomics using StageTips. Nat. Protoc. *2*, 1896–1906.
1130 Redko, Y., Aubert, S., Stachowicz, A., Lenormand, P., Namane, A., Darfeuille,
1131 F., Thibonnier, M., and De Reuse, H. (2013). A minimal bacterial RNase J-
1132 based degradosome is associated with translating ribosomes. Nucleic Acids
1133 Res. *41*, 288–301.
1134 Redko, Y., Galtier, E., Arnion, H., Darfeuille, F., Sismeiro, O., Coppée, J.-Y.,
1135 Médigue, C., Weiman, M., Cruveiller, S., and De Reuse, H. (2016). RNase J
1136 depletion leads to massive changes in mRNA abundance in *Helicobacter pylori*.
1137 RNA Biol. *13*, 243–253.
1138 Schuck, P. (2000). Size-distribution analysis of macromolecules by
1139 sedimentation velocity ultracentrifugation and Lamm equation modeling.
1140 Biophys. J. *78*, 1606–1619.
1141 Sharma, C.M., Hoffmann, S., Darfeuille, F., Reignier, J., Findeiß, S., Sittka, A.,
1142 Chabas, S., Reiche, K., Hackermüller, J., Reinhardt, R., et al. (2010). The
1143 primary transcriptome of the major human pathogen Helicobacter pylori. Nature
1144 *464*, 250–255.
1145 Sievers, F., Wilm, A., Dineen, D., Gibson, T.J., Karplus, K., Li, W., Lopez, R.,
1146 McWilliam, H., Remmert, M., Söding, J., et al. (2011). Fast, scalable generation
1147 of high-quality protein multiple sequence alignments using Clustal Omega. Mol.
1148 Syst. Biol. *7*, 539.
1149 Song, L., Wang, G., Malhotra, A., Deutscher, M.P., and Liang, W. (2016).
1150 Reversible acetylation on Lys501 regulates the activity of RNase II. Nucleic
1151 Acids Res. *44*, 1979–1988.
1152 Tejada-Arranz, A., and De Reuse, H. (2021). Riboregulation in the Major
1153 Gastric Pathogen Helicobacter pylori. Front. Microbiol. *12*, 712804.

1154 Tejada-Arranz, A., de Crécy-Lagard, V., and de Reuse, H. (2020a). Bacterial
1155 RNA Degradosomes: Molecular Machines under Tight Control. Trends
1156 Biochem. Sci. *45*, 42–57.
1157 Tejada-Arranz, A., Galtier, E., El Mortaji, L., Turlin, E., Ershov, D., and De
1158 Reuse, H. (2020b). The RNase J-Based RNA Degradosome Is
1159 Compartmentalized in the Gastric Pathogen Helicobacter pylori. MBio *11*,
1160 e01173-20.
1161 Tejada-Arranz, A., Matos, R.G., Quentin, Y., Bouilloux-Lafont, M., Galtier, E.,
1162 Briolat, V., Kornobis, E., Douché, T., Matondo, M., Arraiano, C.M., et al. (2021).
1163 RNase R is associated in a functional complex with the RhpA DEAD-box RNA
1164 helicase in *Helicobacter pylori*. Nucleic Acids Res.
1165 Tyanova, S., Temu, T., and Cox, J. (2016). The MaxQuant computational
1166 platform for mass spectrometry-based shotgun proteomics. Nat. Protoc. *11*,
1167 2301–2319.
1168 Winn, M.D., Ballard, C.C., Cowtan, K.D., Dodson, E.J., Emsley, P., Evans, P.R.,
1169 Keegan, R.M., Krissinel, E.B., Leslie, A.G.W., McCoy, A., et al. (2011).
1170 Overview of the CCP4 suite and current developments. Acta Crystallogr. D.
1171 Biol. Crystallogr. *67*, 235–242.
1172 Wolfe, A.J. (2016). Bacterial protein acetylation: new discoveries unanswered
1173 questions. Curr. Genet. *62*, 335–341.
1174 Zhao, Y., Lu, M., Zhang, H., Hu, J., Zhou, C., Xu, Q., Ul Hussain Shah, A.M.,
1175 Xu, H., Wang, L., and Hua, Y. (2015). Structural insights into catalysis and
1176 dimerization enhanced exonuclease activity of RNase J. Nucleic Acids Res. *43*,
1177 5550–5559.
1178 Zhou, H.X., and Pang, X. (2018). Electrostatic Interactions in Protein Structure,
1179 Folding, Binding, and Condensation. Chem. Rev. *118*, 1691–1741.
1180